**Article type: Research Article** 

Highly conductive titania supported iridium oxide nanoparticles with low overall iridium density as OER catalyst for large-scale PEM electrolysis

Daniel Böhm, Michael Beetz, Christian Gebauer, Maximilian Bernt, Jonas Schröter, Matthias Kornherr, Florian Zoller, Thomas Bein\* and Dina Fattakhova-Rohlfing\*

Dr. D. Böhm, M. Beetz, Prof. Dr. T. Bein

Department of Chemistry and Center for NanoScience (CeNS), Ludwig-Maximilians-Universität München, Butenandtstrasse 5-13 (E), 81377 Munich, Germany E-Mail: bein@lmu.de

Dr. D. Böhm, F. Zoller, Prof. Dr. D. Fattakhova-Rohlfing Institute of Energy and Climate Research (IEK-1) Materials Synthesis and Processing, Forschungszentrum Jülich GmbH, Wilhelm-Johnen-Strasse, 52425 Jülich, Germany

Prof. Dr. D. Fattakhova-Rohlfing

Faculty of Engineering and Center for Nanointegration Duisburg-Essen (CENIDE), Universität Duisburg-Essen, Lotharstraße 1, 47057 Duisburg, Germany E-Mail: d.fattakhova@fz-juelich.de

Dr. C. Gebauer

Heraeus Deutschland GmbH & Co. KG, Heraeusstr. 12 - 14, 63450 Hanau, Germany

Dr. M. Bernt, J. Schröter, M. Kornherr

Chair of Technical Electrochemistry, Department of Chemistry and Catalysis Research Center, Technical University of Munich, 85748 Garching, Germany

Keywords: supported OER catalyst, PEM electrolysis, homogenous iridium coating, iridium oxide nanoparticles, titania support catalyst

To enable future large-scale generation of hydrogen via proton exchange membrane (PEM) electrolysis, utilization of scarce iridium-based catalysts required for the oxygen evolution reaction (OER) has to be significantly lowered. To address this question, the facile synthesis of a highly active TiO<sub>2</sub> supported iridium oxide based OER catalyst with reduced noble metal content and an Ir-density of the catalyst powder as low as  $0.05 - 0.08 \, \mathrm{g_{Ir} \, cm^{-3}}$  is described in this work. A high surface area corrosion-resistant titania catalyst support homogeneously coated with a 1-2 nm thin layer of amorphous IrOOH<sub>x</sub> is oxidized in molten NaNO<sub>3</sub> between 350-375 °C. This procedure allows for a controllable phase transformation and crystallization

to form a layer of interconnected IrO<sub>2</sub> nanoparticles of  $\approx$ 2 nm on the surface of the TiO<sub>2</sub> support. The increase in crystallinity is thereby accompanied by a significant increase in conductivity of up to 11 S cm<sup>-1</sup> for a 30 wt% Ir loaded catalyst. Oxidized samples further display a significantly increased stability with less detectable Ir dissolution under OER conditions. With a mass-based activity of 59 A g<sup>-1</sup> at an overpotential of 300 mV, the electrocatalytic activity is maintained at the level of the highly active amorphous IrOOH<sub>x</sub> phase used as precursor and outperforms it at higher current densities through the increased conductivity. MEA measurements with catalyst loadings of 0.2-0.3 mg cm<sup>-2</sup> further confirm the high catalytic activity and initial stability at industrially relevant current densities. The introduced synthesis approach therefore shows a path for the fabrication of novel highly active and atom-efficient oxide supported catalysts with complex nanostructures and thin homogenous nanoparticle coatings that allows a future large-scale application of PEM electrolysis technology without restrictions by the natural abundance of iridium.

### 1. Introduction

The awareness of the global warming potential of green-house gases emitted on a large scale by the combustion of carbon based fossil energy carriers has led to enormous investments in renewable energy sources in the last decades.<sup>[1]</sup> Related to the generation and transmission of sustainable electrical energy, mainly intermittent in nature, is its storage which is required to mitigate power fluctuations.<sup>[2]</sup> Among different possibilities, conversion of electrical energy to hydrogen as fuel via electrolysis of water is one of the most economically feasible and sustainable energy storage technologies. Besides the long-established alkaline (KOH-based) and high temperature solid oxide electrolyte electrolyzers, proton exchange membrane (PEM)-electrolyzers enjoy an upswing in the industrial and research interest as prospective conversion technique for decentralized electrical renewable energy generators with high output fluctuations. The key advantages of PEM electrolyzers are their high efficiency, high

applicable current density, capability for intermittent operation, high hydrogen output pressure and compact size.<sup>[3]</sup> However, high investment costs mainly governed by the Nafion® (PEM) membrane, Ti-sinter and the platinum group metals (PGM) Pt (cathode) and Ir (anode)<sup>[4]</sup> used as hydrogen evolution (HER) and oxygen evolution reaction (OER) catalysts, respectively, still limit their widespread application.

Besides economic factors, large-scale deployment of these electrolyzers is hindered by the scarce PGM catalysts.<sup>[5]</sup> Especially iridium, which is employed as an OER catalyst and being mined only as a platinum by-product,<sup>[6]</sup> is in the focus of attention with a projected required 40-fold reduction<sup>[5]</sup> in its utilization. This is also a strong motivation for research on non-noble metal oxides, phospides or sulfides with novel compositions<sup>[7]</sup> and nanomorphologies<sup>[8-10]</sup> that present unforeseen or even rationally designed<sup>[11]</sup> catalytic activity towards the oxygen evolution reaction by the formation of catalytically active sites in these structures.

However, up to date iridium and especially its oxide are still the best compromise of a corrosion-stable and active catalyst material applicable under the harsh oxidizing and acidic environment of a PEM anode.<sup>[12]</sup>

The main challenge to be addressed is therefore the reduction of the iridium mass loading on the anode by increasing the mass-based electrocatalytic activity (determined in A g<sub>Ir</sub><sup>-1</sup>) while maintaining or even increasing the long-term corrosion stability.<sup>[5]</sup> To accomplish this task, several partly complementary approaches were suggested in the literature for Ir-based OER catalysts. As one of the means to increase the electrocatalytic and Ir mass-based activity of catalysts, stabilization of the highly active but less stable<sup>[13]</sup> hydrous IrO<sub>x</sub> phase,<sup>[14]</sup> as well as the preparation of transition metal or fluorine doped ternary<sup>[15-20]</sup> or quaternary<sup>[21-23]</sup> oxide catalysts have been investigated. Another widespread approach to increase the atomefficiency of Ir-based catalysts is an increase of their electrochemically active surface area, achieved either via nanostructuring,<sup>[24-30]</sup> preparation of thin films<sup>[31]</sup> or porous material,<sup>[32-34]</sup>

or via a nanoparticle synthesis approach.<sup>[35]</sup> Finally, the dispersion of the active material on corrosion-stable supports is a strategy explored and already commercialized in recent years. This approach increases the noble metal mass-based activity and furthermore leads to the formation of a catalyst with low volumetric Ir density (packing density) favorable for the preparation of thick and stable electrode layers in PEM electrolyzers with reduced areal Irloading.<sup>[5, 36, 37]</sup>

For applications in the current PEM electrolyzer designs the catalysts layer has to be electrically conducting, which ideally implies electrical conductivity also for the support material to provide continuous charge transport pathways to the current collectors and to minimize ohmic losses. The search for electrically conducting support materials for Ir-based catalysts has been intensive, with reported examples including transparent conductive oxides (TCO) such as antimony doped tin oxide (ATO), [26, 36, 38-40] indium tin oxide (ITO)[41, 42] and fluorine doped tin oxide (FTO)<sup>[40]</sup> or recently investigated carbidic materials such as NbC, TiC, WC<sup>[42]</sup> or TaC, <sup>[43, 44]</sup> which allow for maximum Ir dispersions and show record OER activities due to the provided conductivity. However, none of the materials demonstrated so far sufficient long-term stability under harsh OER conditions (large positive overpotentials and acidic pH values), which is another essential requirement for the PEM catalysts. [36, 45] So far, TiO<sub>2</sub> is the only truly oxidation-stable support material known, and it has been used in chlorine-alkali electrolysis for years as dimensionally stable electrode material (DSA®).<sup>[46]</sup> In recent years TiO<sub>2</sub> was also investigated regarding its use in acidic OER, with favorable particle-support interactions improving the electrocatalytic activity<sup>[47-50]</sup> for diverse nanomorphologies<sup>[49, 51]</sup> and high surface area TiO<sub>2</sub> structures.<sup>[49, 50]</sup> In addition, advances in the maximum possible iridium dispersion and thus reduced loading were made by introducing conductivity in the n-type semiconductor TiO<sub>2</sub> by doping, [52-55] oxynitride formation, [56] hydrogenation<sup>[57]</sup> or by direct formation of substoichiometric conductive Magnéli phases.<sup>[58]</sup>

Undoped, practically non-conductive  $TiO_2$  requires a charge percolation pathway established by interconnected highly conductive  $IrO_2$  domains, with a lower reported threshold for unconstrained OER of  $\approx 1.0 \times 10^{-3}$  S cm<sup>-1</sup>.[59] For a random  $TiO_2/IrO_2$  distribution resulting from intermixing of Ti/Ir precursors, a minimum Ir content of 25 - 30 wt%  $Ir^{[59, 60]}$  for mesoporous structures and  $\approx 55$  wt%  $Ir^{[50, 61]}$  for random structures built from nanoparticles were reported to be required for efficient OER catalysis.

For industrial applications with current densities of several A cm<sup>-2</sup>, the conductivity within the catalyst layer becomes a decisive factor due to the corresponding voltage loss.<sup>[62]</sup> To obtain a TiO<sub>2</sub>-supported catalyst with a macroscopic conductivity of several S cm<sup>-1</sup> and at the same time reduced noble metal loading, a homogeneous distribution and interconnectivity of the nanosized Ir-oxide phase has to be realized. Due to the lack of truly homogeneous coating processes for TiO<sub>2</sub> nanostructures with IrO<sub>2</sub> nanoparticle layers, the state-of-the-art commercially available TiO<sub>2</sub>-supported IrO<sub>2</sub> catalysts (e.g. Elyst Ir75, UMICORE) still have Ir contents of 75 wt%.<sup>[62, 63]</sup>

Here, we report the generation of a novel highly active TiO<sub>2</sub> supported IrO<sub>2</sub> nanoparticle catalyst with only 30 wt% Ir, based on a controlled iridium oxidation process for the formation of a layer of interconnected IrO<sub>2</sub> nanoparticles. High surface area titania is employed as a corrosion-resistant catalyst support that is coated with a thin homogeneous layer of amorphous IrOOH<sub>x</sub>, which is transformed into a more stable IrO<sub>x</sub> phase via thermal treatment.

To increase the corrosion resistance of the hydrous iridium oxide, calcination in air is a valid approach that results in the formation of rutile  $IrO_2$  phase at  $\approx 400$  °C. [64-66] However, this approach suffers from a less controllable and less uniform particle growth with formation of larger isolated  $IrO_2$  crystals on the non-conductive  $TiO_2$  surface, hence interrupting charge percolation pathways.

By applying a precisely controllable oxidation of the material in molten NaNO<sub>3</sub> as proposed by Abbot *et al.*,  $^{[67]}$  a phase transformation and crystallization of uniform IrO<sub>2</sub> nanoparticles can be achieved from an amorphous IrOOH<sub>x</sub> layer employed as iridium precursor phase in this work. Optimizing the synthesis conditions further leads to a mostly continuous layer of interconnected IrO<sub>2</sub> nanoparticles, resulting in a highly active TiO<sub>2</sub>-supported IrO<sub>2</sub> nanoparticle catalyst with significantly increased conductivity and stability. The proposed synthesis pathway thereby allows for a facile preparation and tuneability of the catalyst nanomorphology and surface area (via selection of the respective TiO<sub>2</sub> support), Ir-loading (via the thickness of the applied IrOOH<sub>x</sub> layer) and activity, crystallinity and conductivity (controlled by the parameters of the molten salt oxidation). This novel strategy enables the preparation of Ir-based oxide-supported OER catalysts with optimized iridium dispersion and low Ir-volume density, which are required for the preparation of PEM-electrolyzer anodes with significantly reduced Ir content.

### 2. Results and Discussion

### 2.1 Structural characterization of TiO<sub>2</sub> / IrOOH<sub>x</sub> before and after oxidation

Two batches of IrOOH<sub>x</sub> coated TiO<sub>2</sub> catalyst were obtained from HERAEUS Deutschland GmbH & Co. KG with nominal Ir metal contents of 30 and 45 wt% Ir, respectively, which are designated as "non-heated" catalysts. In a facile and industrially scalable molten salt oxidation in NaNO<sub>3</sub>, the IrOOH<sub>x</sub> coated TiO<sub>2</sub> is oxidized at temperatures of 350, 365, 375 and 400 °C. In the following work, the products obtained by the oxidation of the 30 and 45 wt% Ir containing catalysts are color-coded in the respective plots as shades of red and blue, respectively. Details about the preparation and oxidation procedure are given in the Experimental Section.

X-ray diffraction analysis (**Figure 1**a) of the non-heated 30 wt% Ir containing IrOOH<sub>x</sub>/TiO<sub>2</sub> catalyst (black line) shows reflections with high intensity at the position related to TiO<sub>2</sub>

anatase phase (red reference pattern) and less intensive reflections related to rutile  $TiO_2$  (orange reference pattern) identical to the recorded reference pattern of  $TiO_2$  (grey curve). In addition to the  $TiO_2$  reference, the pattern of the  $IrOOH_x$  coated catalyst shows a very broad increase in intensity centered around  $\approx 33^{\circ} 2\theta$  ranging from the  $TiO_2$  rutile 110 to the 101 reflection. This broad feature is associated with the amorphous or "hydrous"  $IrOOH_x$  phase. [68] Identical reflections are also observed for the 45 wt% Ir coated  $IrOOH_x/TiO_2$  catalyst (**Figure S1**a) with a significantly increased intensity centered around  $\approx 33^{\circ} 2\theta$  ranging from the  $TiO_2$  rutile 110 up to rutile 101 reflection and representing an increased amount of amorphous Ir-phase besides the highly crystalline  $TiO_2$ .

The Raman spectrum shown in Figure 1b further confirms the presence of the major  $TiO_2$  anatase phase for the 30 wt% Ir coated catalyst with a visible  $B_{1g}$  band at  $\approx$ 400 cm<sup>-1</sup>, a  $A_{1g}/B_{2g}$  band at  $\approx$ 520 cm<sup>-1</sup> and the  $E_g$  band at  $\approx$ 640 cm<sup>-1</sup>. [69] Indication for the presence of an additional amorphous Ir-phase is given by the low slope between the  $TiO_2$  anatase  $A_{1g}/B_{1g}$  and  $E_g$  bands, as the  $IrO_2$   $E_g$  band is located at 561 cm<sup>-1</sup>. [70, 71] Similar Raman spectra for the 45 wt% Ir containing catalyst are shown in Figure S1b, although the bands of the  $TiO_2$  anatase phase are even broader with a slightly increased intensity in the region of the  $IrO_2$   $E_g$  band at  $\approx$ 560 cm<sup>-1</sup>. The reduced signal of the  $TiO_2$  phase can be explained by the homogeneous  $IrOOH_x$  or  $IrO_2$  coating, respectively, which significantly decreases the observable Raman scattering of the underlying  $TiO_2$ .

For both Ir coating contents of 30 and 45 wt% (Figure 1b and Figure S1b), a gradual and relative increase in intensity at  $\approx 560 \text{ cm}^{-1}$  can be observed with increasing oxidation temperature in molten NaNO<sub>3</sub>. [70, 71]

Reaction products obtained at oxidation temperatures of 350 - 375 °C indicate crystallization of the IrOOH<sub>x</sub> phase to form an IrO<sub>x</sub> phase that is not fully crystalline and distinct from the tetragonal IrO<sub>2</sub> phase. [67, 68, 72] This intermediate phase with small IrO<sub>x</sub> nanoparticles of about

1 − 2 nm is described in the literature for the molten salt or "Adams fusion" synthesis from Irprecursors in the temperature range of around 350 °C. It only shows one broad bump of intensity around 35°  $2\theta$  in the X-ray diffractograms (Figure 1a and Figure S1). [50, 61, 73] The broad diffraction peak thereby cannot be assigned to the 101 rutile IrO<sub>2</sub> lattice plane or any other Ir phase but rather represents a pair distribution function originating from an amorphous or disordered IrO<sub>x</sub> phase with a reported Ir-O atomic distance of ≈2.03 Å determined from EXAFS measurements. [67, 72]

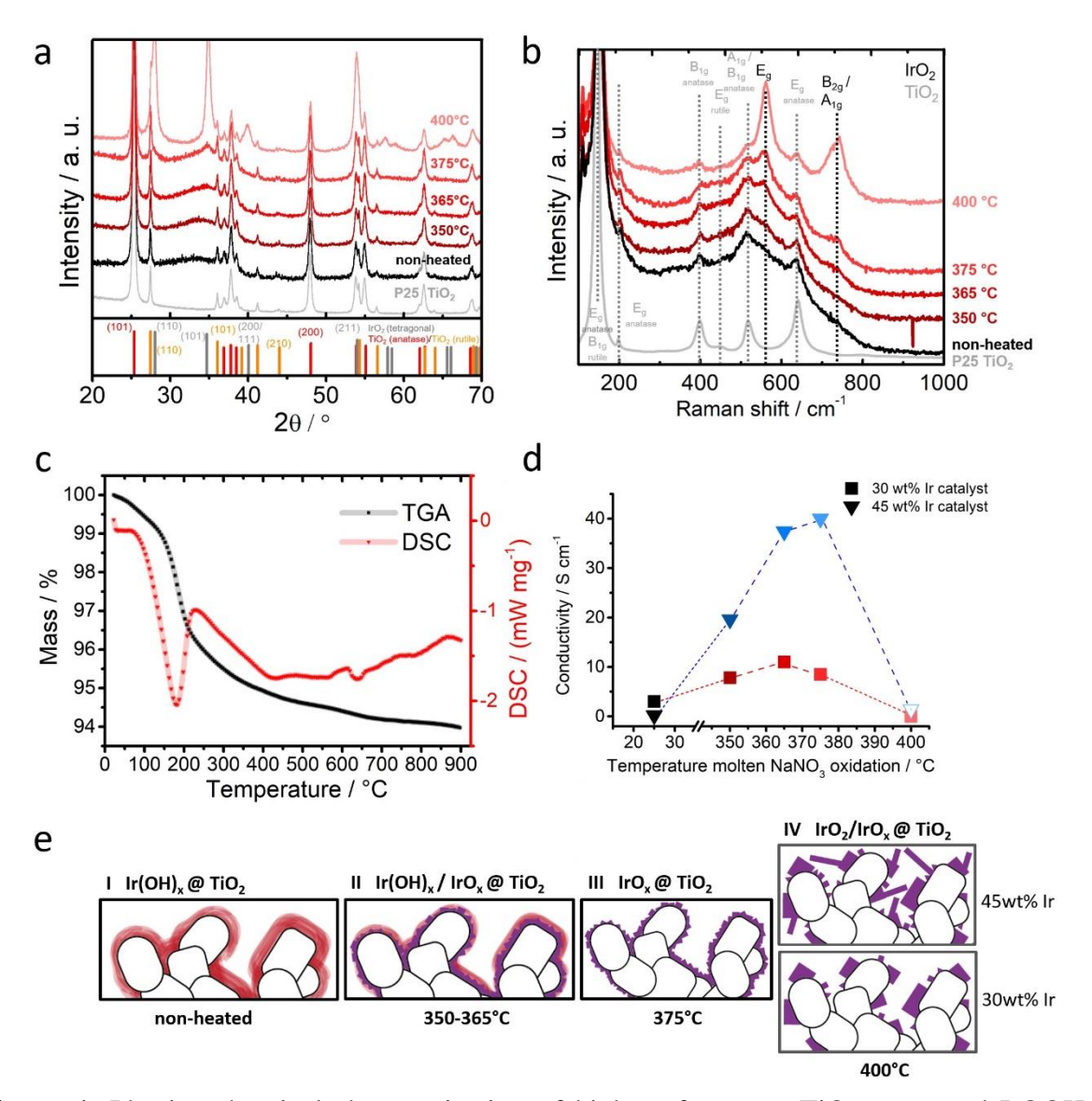


**Figure 1.** Physico-chemical characterization of high surface area TiO<sub>2</sub> supported IrOOH<sub>x</sub>, IrO<sub>x</sub> and IrO<sub>2</sub> with a total loading of 30 wt% Ir after oxidation at various temperatures, with scheme of Ir coating nanostructure. (a) X-ray diffraction patterns and (b) Raman spectra of

IrOOH<sub>x</sub> coated TiO<sub>2</sub> before (black curve) and after oxidation in molten NaNO<sub>3</sub> at temperatures between 350 - 400°C (dark-red to light red curves). IrO<sub>2</sub> pattern: ICDD card number 00-015-0870 (grey) (tetragonal symmetry, a = b = 4.4983 Å, c = 3.1544 Å,  $\alpha = \beta = \gamma = 90^{\circ}$ ). TiO<sub>2</sub> (anatase) (ICDD card number 00-004-0477, tetragonal symmetry, a = b = 3.783 Å, c = 9.510 Å,  $\alpha = \beta = \gamma = 90^{\circ}$ ) and TiO<sub>2</sub> (rutile) (ICDD card number 00-004-0551, tetragonal symmetry. a = b = 4.594 Å, c = 2.958 Å,  $\alpha = \beta = \gamma = 90^{\circ}$ ). Raman bands at 561 cm<sup>-1</sup> (E<sub>g</sub>) and close bands at 728 cm<sup>-1</sup> (B<sub>2g</sub>) and at 752 cm<sup>-1</sup> (A<sub>1g</sub>) correspond to the tetragonal iridium oxide phase. [70, 71] Raman bands at 144 cm<sup>-1</sup> (E<sub>g</sub>), 197 cm<sup>-1</sup> (E<sub>g</sub>), 399 cm<sup>-1</sup> (B<sub>1g</sub>), 519 cm<sup>-1</sup> (A<sub>1g</sub>/B<sub>1g</sub>) and 639 cm<sup>-1</sup> (E<sub>g</sub>) correspond to anatase TiO<sub>2</sub> and bands at 143 cm<sup>-1</sup> (B<sub>1g</sub>) and 447 cm<sup>-1</sup> (E<sub>g</sub>) were assigned to rutile TiO<sub>2</sub>. [63] (c) Thermogravimetric analysis with differential scanning calorimetry. (d) Specific conductivities of non-heated and oxidized catalyst powder samples of 30 (red squares) and 45 wt% Ir (blue triangles) coated TiO<sub>2</sub> catalyst. (e) Schematic representation of IrOOH<sub>x</sub>/TiO<sub>2</sub> catalyst nanostructure formation after oxidation at various temperatures for low (30 wt%) and high (45 wt%) Ir loading.

Oxidation at 400 °C leads, for both Ir loadings, to a significant increase in crystallinity indicated by the formation of the rutile IrO<sub>2</sub> phase with average domain sizes of  $\approx$ 18 nm and  $\approx$ 27 nm for the 30 and 45 wt% containing TiO<sub>2</sub> supported catalyst, respectively (calculated from the 101 reflection broadening with the Scherrer equation).<sup>[74]</sup>

The significantly enhanced crystallization at 400 °C - exceeding the expected influence of the sole temperature difference compared to an oxidation at 375 °C - is attributed to a decomposition of the NaNO<sub>3</sub> melt starting at that temperature. According to literature, thermal decomposition of NaNO<sub>3</sub> consists of three successive or concurrent reactions and processes that include a nitrate to nitrite plus oxygen reaction as well as thermal evaporation. The decomposition temperature of NaNO<sub>3</sub> thereby depends on the exact reaction parameters (heating rate, atmosphere, crucible etc.) with reported values ranging from 380 °C to 450 °C and above. [75-77] The low boiling point of NaNO<sub>3</sub> of  $T_b$ =380 °C and the partial decomposition of NO<sub>3</sub>- to NO<sub>2</sub> +  $\frac{1}{2}$  O<sub>2</sub> + e- thereby lead to strong oxidizing conditions in contrast to the

lower O<sub>2</sub> partial pressure present in molten NaNO<sub>3</sub> at lower temperatures, resulting in a limited particle growth.<sup>[75-77]</sup>

The Raman spectrum for 45 wt% Ir coated  $TiO_2$  (IrOOH<sub>x</sub> oxidized at 400 °C) (Figure S1b) does not even show distinct reflections as the bands are further broadened. This can be explained by the complete coverage of the  $TiO_2$  by  $IrO_2$  on the one hand, and by the very low signal intensities resulting from a significantly increased optical absorption of the sample on the other hand.

The phase transformation of amorphous 30 wt% Ir containing IrOOH<sub>x</sub>/TiO<sub>2</sub> to IrO<sub>2</sub>/TiO<sub>2</sub> was further investigated by thermogravimetric analysis (TGA) and differential scanning calorimetry (DSC) shown in Figure 1c, and is in accordance with results obtained by Cruz *et al.*<sup>[68]</sup> In the first temperature range up to  $\approx$ 150 °C the IrOOH<sub>x</sub> phase is physically dehydrated which accounts for  $\approx$ 1 wt% of the sample. In the second temperature regime from 150 – 240 °C, further crystal-bound water and hydroxyl groups are removed from the amorphous IrOOH<sub>x</sub> phase and a disordered IrO<sub>x</sub> phase is formed. This electrochemically active phase gradually increases in crystallinity up to  $\approx$ 400 °C in the third temperature regime to finally form the rutile IrO<sub>2</sub> phase, which is in agreement with literature reports. <sup>[64]</sup> Temperatures above 400 °C lead to a further crystallization and growth of initially formed small and defect rich IrO<sub>2</sub> domains to stoichiometric bulk IrO<sub>2</sub>, which is reflected by a minor mass loss below 1 wt% in the range up to 900 °C.

A key factor for the application of the oxidized IrOOH<sub>x</sub>/TiO<sub>2</sub> catalyst in PEM electrolyzers is its conductivity, which was measured with compressed powder pellets with a 4-point probe conductivity and Hall-effect measurement device. Based on the observed trends in the conductivity with the calcination temperature shown in Figure 1d for 30 wt% (shades of red) and 45 wt% (shades of blue) Ir containing catalyst, together with the results of electron microscopy, X-ray diffraction and Raman spectroscopy we have proposed a crystallization

mechanism schematically depicted in Figure 1e, which will be addressed in more detail below.

The conductivity of hydrous iridium oxide (precursor phase) as well as other hydrous oxides and their crystalline counterparts (rutile IrO<sub>2</sub> after oxidation at temperatures of >400 °C) thereby differ fundamentally in their magnitude and underlying mechanism. For the hydrous iridium oxide phase, the electrical conductivity within the electrode layer is a sum of the electronic conductivity of the material and contribution by the ionic conductivity given by proton or hydroxide diffusion through the amorphous structure.<sup>[78-79]</sup> According to Burke et al. the electronic conductivity of hydrous iridium oxide with respect to the level of hydration can thereby be explained by a variation in the length of weakly cross-linked conducting polymer chains in the hydrous matrix (interrupted strand model).<sup>[78]</sup> However, for a high degree of hydration (such as the non-heated IrOOH<sub>x</sub> product with amorphous structure) with short IrOH<sub>x</sub> chains the electronic conductivity is decreased due the sum of the charge transfer resistance between the individual chains which increases the contribution of the ionic conductivity in the material. [80] Heat-treatment between 100 - 300 °C dehydrates the structure without a significant increase in crystallinity, causing a decrease in ionic conductivity without an significant increase in the electronic conductivity.<sup>[45]</sup> In the temperature range above (350) – 400 °C) a slow crystallization of the dehydrated amorphous IrO<sub>x</sub> structure resulting in the rutile IrO<sub>2</sub> phase is observed, which significantly increases the conductivity via the formation of a metal-like band structure through overlap of the Ir-4d and O-2p orbitals.<sup>[45, 81]</sup> For the 30 wt% IrOOH<sub>x</sub>/TiO<sub>2</sub> catalyst a conductivity of ≈3.0 S cm<sup>-1</sup> (Figure 1d, black square and Figure 1e, step I) for the non-heated material is high when compared to literature values of up to  $1.5 \times 10^{-2}$  S cm<sup>-1</sup> reported for electro-flocculated 2 nm sized IrO<sub>x</sub> particles.<sup>[82]</sup> However, the conductivity of hydrous iridium oxide is significantly influenced by the morphology, degree of hydration and the oxidation state of iridium. This leads to a broad range of reported conductivity values ranging from  $10^{-6}$  S cm<sup>-1</sup> for IrO<sub>x</sub> nanoparticles with Ir in oxidation state +III up to an apparent conductivity of  $8.1 \times 10^{-1}$  S cm<sup>-1</sup> for an ATO supported IrO<sub>x</sub> nanoparticle catalyst with a conductivity of  $1.8 \times 10^{-2}$  S cm<sup>-1</sup> determined for the ATO support only, which indicates an even higher conductivity of the IrO<sub>x</sub> nanoparticle phase. [64, 82, 83] The high conductivity value measured for the 30 wt% Ir containing sample is attributed to the presence of a very thin hydrated IrOOH<sub>x</sub> layer (as shown by electron microscopy in following sections) on the TiO<sub>2</sub> support and a possible beneficial (hydrous)metal-support interaction leading to an increased conductivity. [47, 48]

Thicker IrOOH<sub>x</sub> layers formed in the case of non-heated 45 wt% Ir containing IrOOH<sub>x</sub>/TiO<sub>2</sub> catalyst exhibit a slightly lower conductivity reaching 0.2 S cm<sup>-1</sup> (Figure 1d, black triangle and Figure 1e, step I), which might be explained by a lower degree of hydration.

Upon oxidation and the associated increase in crystallinity, the conductivity significantly increases to reach a maximum of  $11 \text{ S cm}^{-1}$  at  $365 \,^{\circ}\text{C}$  for the  $30 \,\text{wt}\%$  Ir catalyst and  $40 \,\text{ S cm}^{-1}$  at  $375 \,^{\circ}\text{C}$  for the  $45 \,\text{wt}\%$  Ir containing catalyst (Figure 1d and Figure 1e, step II and III), which agrees well with a reported conductivity of  $\approx 26 \,\text{ S cm}^{-1}$  for a layer of about  $2-3 \,\text{ nm}$  IrO<sub>2</sub> nanoparticles. [84] The values are of the same order of magnitude as an industrial IrO<sub>2</sub>/TiO<sub>2</sub> reference catalyst (Elyst Ir75, UMICORE) [62, 63] with 75 wt% Ir content, with a determined conductivity of 73.1 S cm<sup>-1</sup> under the same measurements conditions. The higher absolute conductivity as well as the higher temperature optimum for the  $45 \,\text{ wt}\%$  Ir containing catalyst compared to the  $30 \,\text{ wt}\%$  Ir containing sample can be explained by the possible formation of larger IrO<sub>2</sub> nanocrystals from the precursor IrOOH<sub>x</sub> phase as depicted in Figure 1e, step III. For both Ir loadings a mostly interconnected layer of highly conductive IrO<sub>2</sub> nanoparticles on top of the non-conductive TiO<sub>2</sub> support is formed in this step, albeit at slightly different temperatures.

Above the temperature optimum, the further growth of  $IrO_2$  particles via Ostwald ripening, consuming surrounding  $IrOOH_x$  and smaller  $IrO_x$  crystals, results in the formation of larger isolated  $IrO_2$  crystals. The formation of isolated particles with high crystallinity (although they are regarded to have a higher conductivity) significantly lowers the overall conductivity of the electrode due to missing charge percolation pathways as depicted in Figure 1e, step IV. The higher amount of  $IrOOH_x$  precursor phase in the 45 wt% Ir containing samples allows for the formation of larger  $IrO_2$  crystals that still enable charge percolation and are not fully isolated in the case of 400 °C oxidized samples. Hence, a reasonable conductivity of  $1.4 \text{ S cm}^{-1}$  is retained for the 45 wt% sample as compared to a significant loss in conductivity with  $4.9 \times 10^{-4} \text{ S cm}^{-1}$  for the 30 wt% Ir containing catalyst.

The proposed scheme in Figure 1e is supported by structural characterization by scanning electron microscopy shown in **Figure 2 and Figure S2-3** for the 30 and 45 wt% Ir containing catalyst samples. The morphology of the non-heated 30 wt% Ir containing IrOOH<sub>x</sub>/TiO<sub>2</sub> exactly matches that of the uncoated TiO<sub>2</sub> structure. The latter is composed of aggregates and larger agglomerates of about 20 – 30 nm primary TiO<sub>2</sub> crystals (Figure 2a,c), which are mainly composed of anatase phase with a minor contribution of rutile TiO<sub>2</sub> (Figure 1a). To assess the coverage of the TiO<sub>2</sub> substrate by the iridium phase, all sample areas were imaged once by scanning with a secondary electron (SE) sensitive detector (Figure 2a,c,e,g,i,k) for morphological contrast and further imaged with a detector sensitive towards backscattered electrons (BSE) for enhanced material contrast (Figure 2b,d,f,h,j,l).

From the comparison of the backscattered electron-based SEM images depicted in Figure 2b,d with the morphology shown in Figure 2a,c and the respective diffractogram (Figure 1a, black curve), a homogeneous coverage of the TiO<sub>2</sub> nanostructure with a thin amorphous IrOOH<sub>x</sub> phase is suggested. From the scanning electron microscopy images shown in Figure S2 and Figure 1e-h it can also be concluded that oxidation at 350 °C, 365 °C

and up to 375 °C in molten NaNO<sub>3</sub> does not alter the morphology of the Ir coated catalyst or affects the homogeneous coverage of the TiO<sub>2</sub> by the formed IrO<sub>x</sub> nanoparticle (Figure 1a,b) layer.

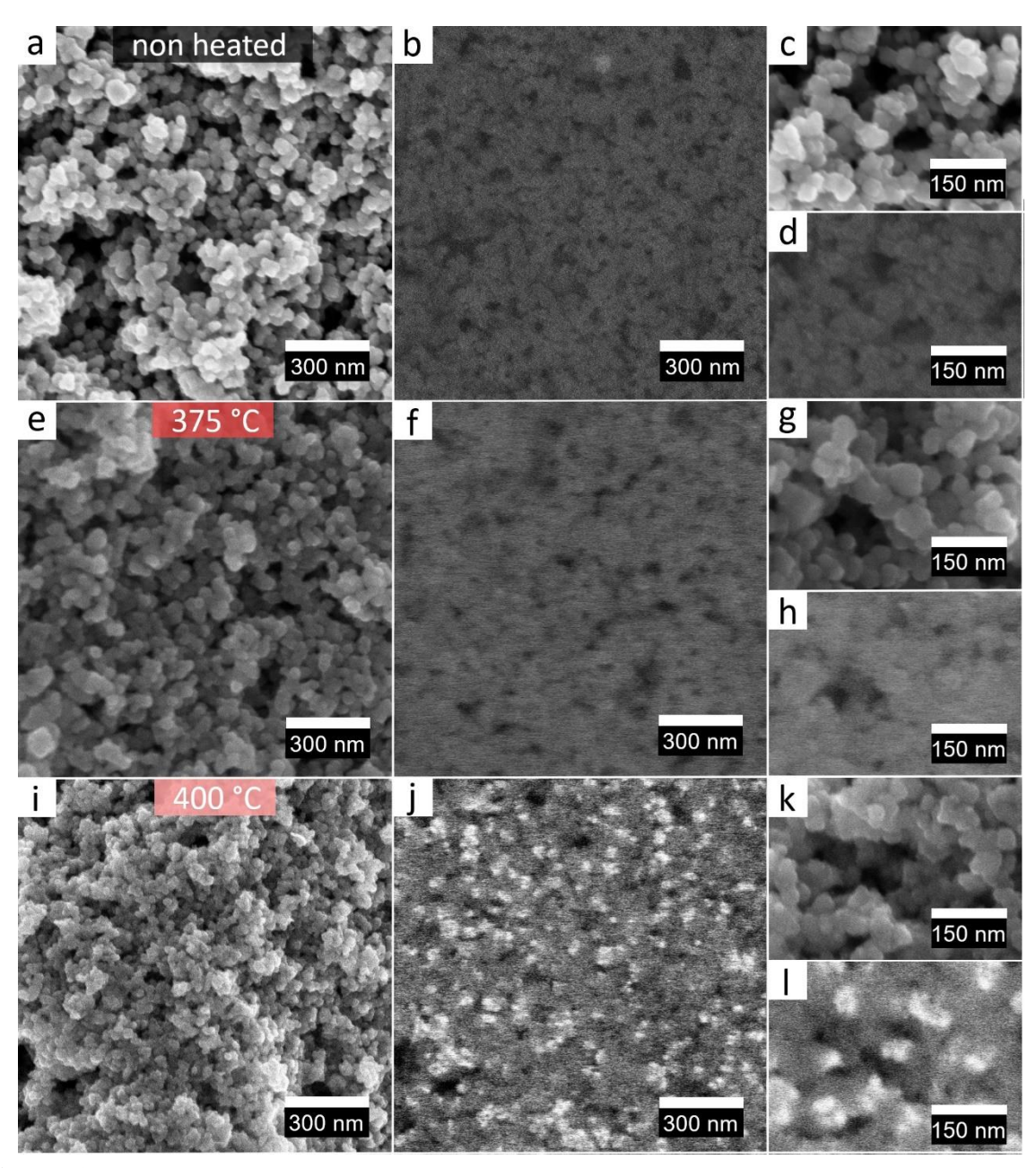


**Figure 2.** SEM images of  $IrO_x$  and  $IrO_2$  nanoparticles on  $TiO_2$  with 30 wt% Ir content. Variation in oxidation temperature of  $IrOOH_x$ -coated  $TiO_2$  from non-heated (a-d) over 375 °C (e-h), 400 °C (i-l) in NaNO<sub>3</sub>. All sample areas were imaged once by recording with a secondary electron sensitive detector (a,c,e,g,i,k) for morphological contrast and further imaged with a detector sensitive towards backscattered electrons for enhanced material contrast (b,d,f,h,j,l).

At an oxidation temperature of 400 °C the morphology of the TiO<sub>2</sub> is still maintained (Figure 2i,k) but the IrO<sub>x</sub>/IrO<sub>2</sub> nanoparticle phase (Figure 1a,b) visibly forms larger aggregates and crystals of several tens of nanometers, as shown by the light spots in the backscattered electron-based SEM images (Figure 2j,l), which were already indicated by the respective XRD patterns (Figure 1a and Figure S1).

The 45 wt% Ir containing IrOOH<sub>x</sub>/TiO<sub>2</sub> catalyst series also exhibits the morphology of the unloaded TiO<sub>2</sub> up to an oxidation temperature of 375 °C (Figure S3a,c,e,g,i,k,m,o), although a slightly rounded shape and increased thickness of the particles (Figure S3a,c) indicate a smooth coverage by the IrOOH<sub>x</sub> phase (Figure S1a,b). In contrast to the 30 wt% Ir containing catalyst sample series, the homogeneity of the coverage with the Ir active phase for the 45 wt% Ir catalyst series seems to be slightly reduced, as small intensity variations across the scan area in the respective backscattered electron based SEM images are visible (Figure S3b,d,f,h,j,l,n,p). In addition, for 45 wt% Ir catalyst samples the formation of a mostly continuous IrOOH<sub>x</sub> and IrO<sub>x</sub>/IrO<sub>2</sub> particle layers at temperatures of up to 375 °C can directly be observed in the high-resolution BSE-based SEM images (Figure S3d,h,l,p) by lighter rims around the TiO<sub>2</sub> nanocrystals.

Oxidation at 400 °C leads to a significantly altered morphology, being composed of the underlying TiO<sub>2</sub> structure with needle-like and particle-like nanostructures on the surface (Figure S3q,s). A comparison with the acquired backscattered electron-based SEM images further confirms the formation of IrO<sub>x</sub>/IrO<sub>2</sub> (Figure S1a,b) needle-like structures shown as brighter features on the underlying TiO<sub>2</sub> structure (Figure S3r,t).

To investigate the phase transformation of amorphous  $IrOOH_x$  to  $IrO_x$  nanoparticles and the coverage of the  $TiO_2$  nanocrystals at the local scale, high resolution scanning transmission electron microscopy (STEM) and energy dispersive X-ray spectroscopy (EDX) were performed.

**Figure 3**a-d shows the larger agglomerated  $TiO_2$  nanocrystals with a dimension of about 20 - 30 nm that are homogeneously coated with a 1 - 2 nm thin amorphous  $IrOOH_x$  phase, visible as a bright diffuse rim around the titania. The electron diffraction pattern (Figure 3d) only shows a diffuse ring that cannot be associated with metallic Ir or a  $IrO_2$  phase, but which agrees well with the X-ray diffraction pattern (Figure 1a) and can be assigned to the amorphous or "hydrous"  $IrOOH_x$  phase. [68]

The visualization of thin amorphous IrOOH<sub>x</sub> layers is possible only under low-dose imaging conditions with short acquisition times, otherwise an electron beam-induced crystallization with the formation of 1 - 2 nm sized particles can be observed after only seconds of illumination (**Figure S4**).

Upon oxidation in molten NaNO<sub>3</sub> at 365 °C, the continuous amorphous layer of the 30 wt% Ir containing catalyst partially crystallizes with the formation of 1 - 2 nm small IrO<sub>x</sub> particles embedded in a surrounding amorphous IrOOH<sub>x</sub> phase, as observed in high resolution STEM images (**Figure S5**b,c,d) and high resolution TEM images (Figure S5a). At a slightly higher oxidation temperature of 375 °C the crystallinity of the IrO<sub>x</sub> layer increases but the layer continuity remains preserved to a large extent. The corresponding STEM images show that the TiO<sub>2</sub> crystal facets (Figure 3e,f) are covered by a mostly interconnected layer of about 2 nm sized IrO<sub>x</sub> nanocrystals (Figure 3g,h).

The further increase in oxidation temperature to 400 °C dramatically alters the catalyst morphology, as already indicated by the XRD, SEM and conductivity measurements discussed above. STEM images and EDX mapping of IrOOH<sub>x</sub>/TiO<sub>2</sub> samples oxidized at 400 °C show that the supporting oxide remains unaltered, but now the titania crystals are covered by isolated and aggregated 1 – 2 nm sized particles as well as longer rod-like crystals (Figure 3i-k,m). According to the electron diffraction pattern depicted in Figure 31, the nanoparticles and rod-like crystals can both be assigned to the rutile IrO<sub>2</sub> phase. The

formation of larger rod-like IrO<sub>2</sub> crystals resulting from a preferential growth along the [001] and [112] directions of the rutile unit cell was described by Abbott *et al.* for IrO<sub>2</sub> synthesized by the Adams fusion method at temperatures above 500 °C, and explained by a thermodynamically favorable formation of 110 surface terminations.<sup>[67]</sup>

STEM imaging of the 45 wt% Ir containing  $TiO_2$  supported sample series shown in **Figure S6** features a similar microstructural evolution of the  $IrOOH_x$  phase upon oxidation in NaNO<sub>3</sub>.

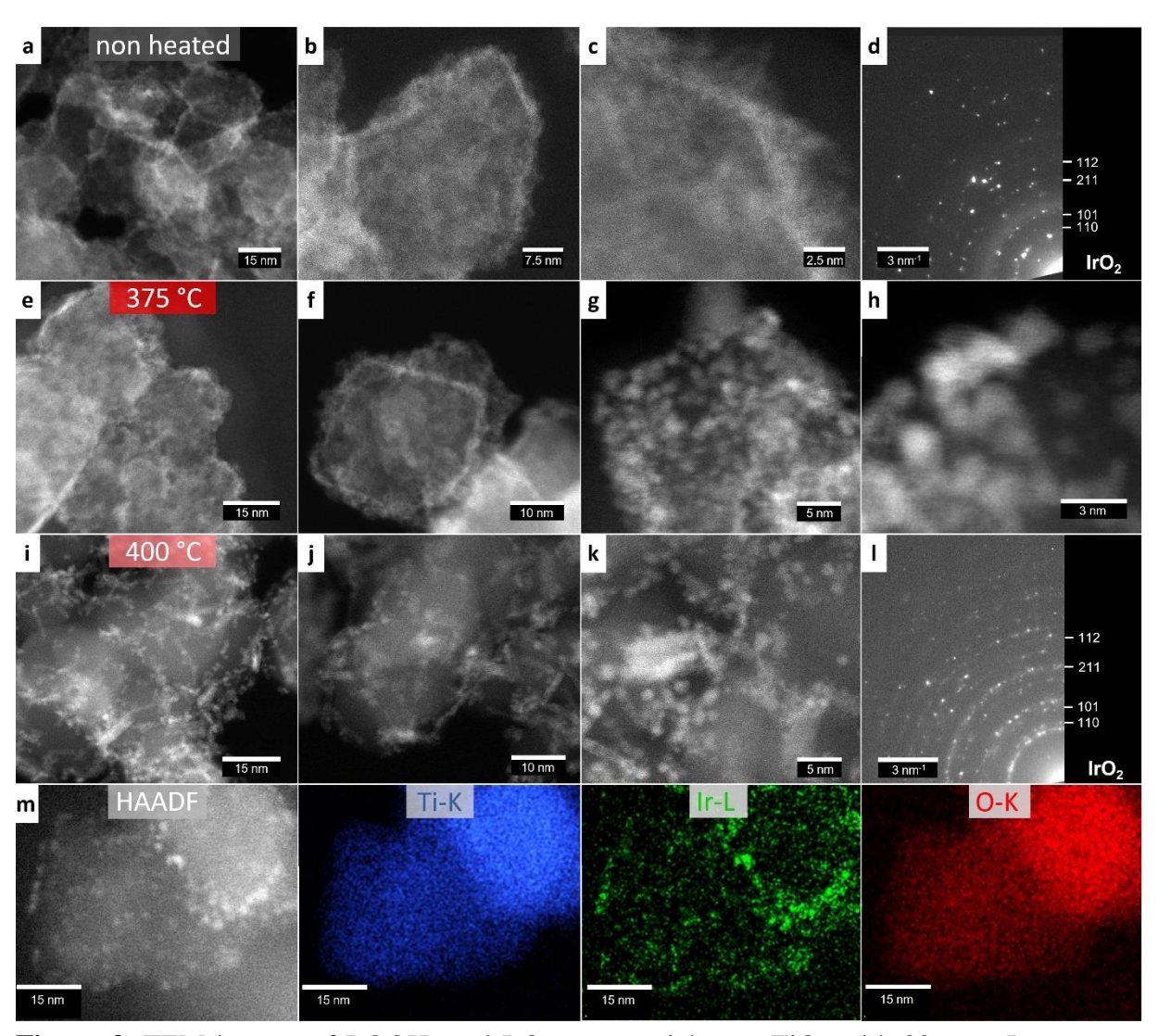


**Figure 3.** TEM images of IrOOH<sub>x</sub> and IrO<sub>2</sub> nanoparticles on TiO<sub>2</sub> with 30 wt% Ir content. Variation in oxidation temperature of IrOOH<sub>x</sub> coated TiO<sub>2</sub> from non-heated (a-d) over 375 °C (e-h) to 400 °C (i-m) in NaNO<sub>3</sub>. Phase identification and assignment of lattice planes in electron diffraction pattern (d,l) according to literature values. IrO<sub>2</sub> pattern: ICDD card

number 00-015-0870 (grey) (tetragonal symmetry, a = b = 4.4983 Å, c = 3.1544 Å,  $\alpha = \beta = \gamma = 90^{\circ}$ ). (m) STEM/EDX elemental mapping of aggregated IrO<sub>2</sub> nanoparticles on TiO<sub>2</sub> nanocrystals after oxidation at 400 °C.

The non-heated IrOOH<sub>x</sub>/TiO<sub>2</sub> sample (Figure S6a-c) displays a rather homogeneous coating with a 5-10 nm thick amorphous Ir-containing phase as indicated by EDX mapping (Figure S6e) and electron diffraction patterns, and which only shows diffraction spots related to TiO<sub>2</sub> anatase and rutile phase (Figure S6d). The microstructure of the 45 wt% catalyst oxidized at 375 °C appears very similar to the lower-loaded counterpart with 1-2 nm  $IrO_x$ mostly interconnected particles attached to the surface of the TiO<sub>2</sub> crystals (Figure S6f-h). The particles are homogeneously distributed on the TiO<sub>2</sub> as shown by EDX mapping (Figure S6j) and consist of an intermediate phase IrO<sub>x</sub> and rutile IrO<sub>2</sub> as shown by the electron diffraction pattern (Figure S6i). Finally, an oxidizing temperature of 400 °C leads to the formation of  $IrO_2$  nanorods and aggregates of small particles sized about 1-2 nm, similar to those observed for the 30 wt% loaded catalyst. However, the length of the nanorods significantly exceeds that of the lower-loaded sample with dimensions of up to about 100  $\times$ 10 nm (Figure S6k), which is also in agreement with the larger average crystalline domain size of  $\approx$ 27 nm determined from XRD line broadening. Although the homogeneity of the Ir distribution is lowered as shown by EDX mapping (Figure S60), the larger rod-like structures still seem to connect isolated particle aggregates on the non-conductive TiO<sub>2</sub> (Figure S6k-n) in contrast to the 400 °C oxidized 30 wt% Ir containing catalyst. The results shown by electron microscopy therefore support the structural model shown in Figure 1e with implications on the conductivity as shown in Figure 1d.

Besides the morphological changes shown by SEM and TEM, the iridium content of the differently oxidized samples remained constant with ~28 wt% Ir for the nominal 30 wt% Ir containing catalyst samples (see **Table S1-3** for further details) and ~52 wt% Ir for the

nominal 45 wt% Ir containing samples (**Table S4-5**). Deviations of the EDX derived Ir content from the nominal Ir content derived from elemental analysis (of the unheated TiO<sub>2</sub>/IrOOH<sub>x</sub>) can be explained by a differing (but consistent) quantification by the employed EDX detection system and its underlying structural model which is not specified for nanometer sized core-shell-like morphologies. Another explanation for the difference of the local Ir loading probed by SEM/EDX to the stated nominal values obtained by elemental analysis can be given by a certain inhomogeneity resulting from the industrial-type kilogram scale synthesis method of the catalyst.

## 2.2 Electrochemical characterization by rotating disc and liquid cell measurements

To investigate the redox activity of the differently oxidized TiO<sub>2</sub> supported Ir-phases, cyclic voltammograms were recorded over a broad potential range between the hydrogen evolution reaction (HER) and OER onset potentials (0.05-1.52 V vs. RHE) before each rotating disc electrode activity measurement (Figure 4a). Besides the OER onset above about 1.45 V vs. RHE, the non-heated 30 wt% Ir containing IrOOH<sub>x</sub>/TiO<sub>2</sub> sample shows a broad peak centered around 0.8 V vs. RHE attributed to the Ir(III)/Ir(IV) redox reaction in acidic environment. [85, <sup>86]</sup> In addition a smaller redox feature (so called pre-peak) at around 0.4 V vs. RHE is shown for the non-heated product and associated with an oxidation of Ir(III) sites close to the metal/oxide interface.<sup>[64]</sup> This feature is reduced in intensity for the IrO<sub>x</sub>/TiO<sub>2</sub> sample oxidized at 375 °C and not further detectable for the IrO2/TiO2 sample prepared at 400 °C (Figure 4a). The reduction in intensity of the respective redox features is thereby directly correlated to an increase in crystallinity with an accompanied decrease of Ir(III) species as present in hydrous iridium oxide (non-heated and oxidized samples below 400 °C) towards the presence of Ir(IV) in rutile IrO<sub>2</sub> which does not show a redox activity below the OER onset as reported in the literature. [64, 67] In addition, a decrease of the peak currents and an overall reduction of the capacitive current all over the scanned potential range can be explained by a decrease of electrochemical surface area correlated with an increase in crystallinity and particle growth at higher oxidation temperatures.<sup>[67]</sup>

The presence and reduction of the Ir(III)/Ir(IV) redox feature upon oxidation is even more pronounced in the cyclic voltammograms of the 45 wt% Ir sample series (**Figure S7**a) due to the increased thickness of the initial amorphous IrOOH<sub>x</sub> layer with bulk redox activity.<sup>[64]</sup> The fact that for the 400 °C oxidized sample still a small Ir(III)/Ir(IV) redox feature is visible indicates a non-complete oxidation of the IrOOH<sub>x</sub> phase to rutile IrO<sub>2</sub>. It is assumed that the higher initial IrOOH<sub>x</sub> layer thickness in the 45 wt% Ir containing sample prevents a complete oxidation under the given synthesis conditions at 400 °C.

To assess the OER onset potential (defined at 1 mA cm<sup>-2</sup>) and catalytic activity under controlled reaction parameters (see Experimental section for details) rotating disc electrode measurements with repeated cyclic voltammetry were performed as shown in Figure 4bc and **Figure S8**ab for the 30 wt% Ir containing sample series. The non-heated IrOOH<sub>x</sub>/TiO<sub>2</sub> catalyst sample exhibits an onset potential of only 202 mV which is in the expected range of a highly OER active hydrous Ir-oxide.<sup>[26,87]</sup>

Interestingly, with the oxidation in molten NaNO<sub>3</sub> the onset potential remains low at 204 mV (365 °C) – 206 mV (375 °C) compared to 252 mV determined for the more crystalline  $IrO_2/TiO_2$  reference catalyst (Elyst Ir75, UMICORE) under same measurements conditions (**Figure S9**a-c). The low onset potential values compare well with the best catalysts reported in the literature, in spite of the comparably low surface area (~55 m<sup>2</sup> g<sup>-1</sup>) and insulating character of the undoped titania substrate used in this work. Thus, a similar low onset potential of 200 mV was reported by Hu *et al.* for a supported catalyst with a comparable Ir loading but evidently more beneficial electrically conducting Nb-doped TiO<sub>2</sub> (NTO) support with a higher surface area ( $\approx$ 83 m<sup>2</sup> g<sup>-1</sup>). Apparently, a conductive NTO support, even with a homogeneous  $IrO_2$  coverage, does not necessarily translate into a lower onset potential as

shown by Hufnagel *et al.* for an 8 wt% Ir coated catalyst with an  $\eta_{OER}$ =250 mV.<sup>[53]</sup> In contrast to the samples oxidized at lower temperatures, oxidation of 30 wt% Ir containing catalyst at 400 °C leads to a significantly increased onset potential of initially 328 mV (5<sup>th</sup> RDE cycle) that rises from the 30<sup>th</sup> cycle up to 532 mV after 75 cycles due to its limited conductivity (Figure 4b,c).

The 45 wt% Ir sample series exhibits a slightly higher onset potential of 211 mV for the non-heated IrOOH<sub>x</sub>/TiO<sub>2</sub> catalyst that also remains low upon oxidation with values of 214 mV (365 °C) – 208 mV (375 °C) (Figure S7b). Samples oxidized at 400 °C still exhibit a relatively low onset potential of 231 mV after 75 RDE scan cycles, which can be explained by the retained conductivity compared to the similarly oxidized 30 wt% Ir sample (Figure S7 and Figure 1).

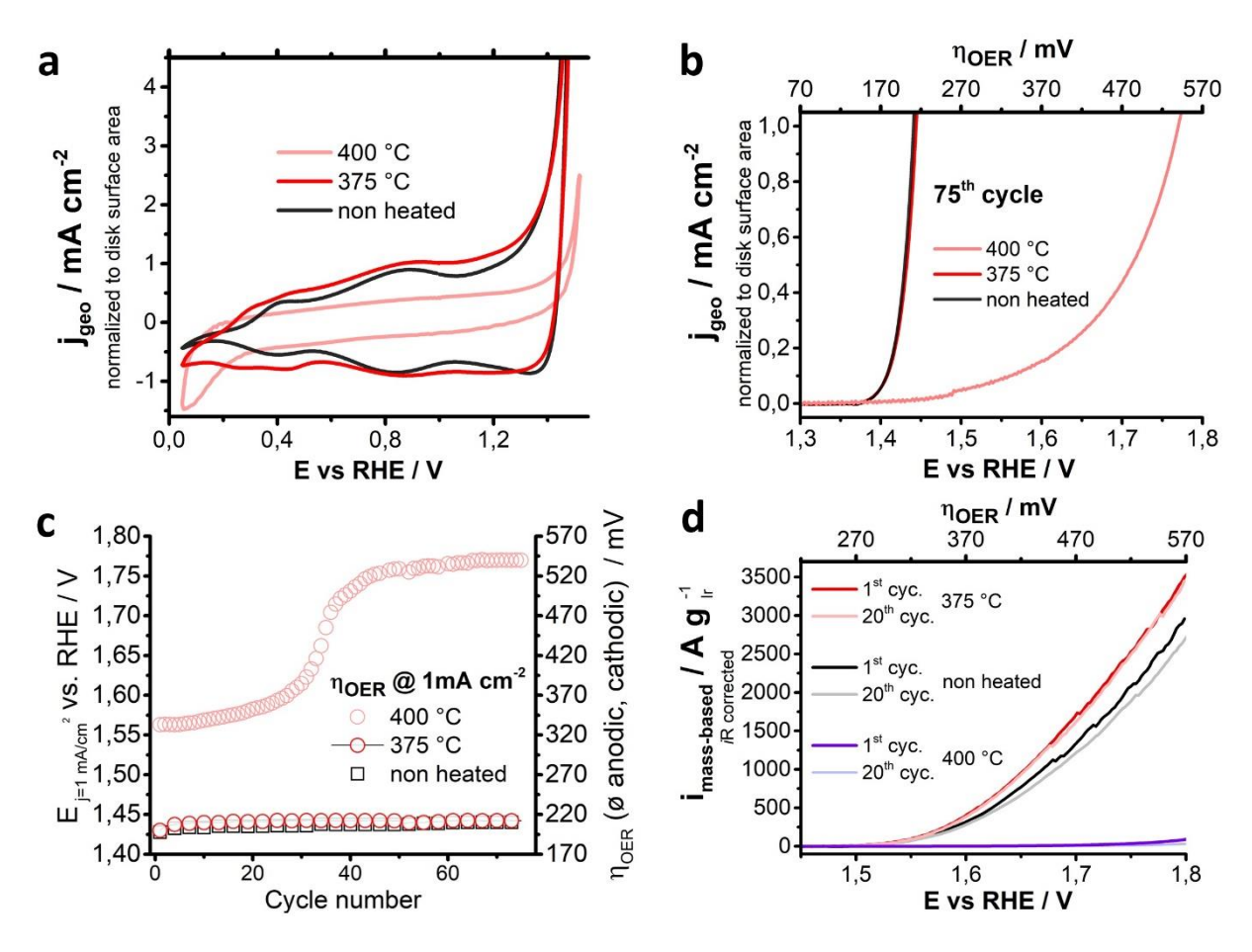


**Figure 4.** Electrochemical characterization of IrOOH<sub>x</sub> and IrO<sub>2</sub> nanoparticles on TiO<sub>2</sub> with 30 wt% Ir content. (a) Cyclic voltammogram between 0.05-1.50 V vs. reversible hydrogen reference electrode (RHE) of IrOOH<sub>x</sub> coated TiO<sub>2</sub> before (black curve) and after oxidation at 375 °C (dark red curve) and 400 °C (light red curve) with a scan rate of 50 mV s<sup>-1</sup>. (b) 75<sup>th</sup> scan cycle of rotating disc electrode measurements for non-heated IrOOH<sub>x</sub>/TiO<sub>2</sub> catalyst (black curve) and 375 °C (red curve) and 400 °C (light red curve) oxidized catalyst. (c) Extracted overpotentials ( $η_{OER}$ ) of RDE measurements for each cycle required to reach a current density of 1 mA cm<sup>-2</sup>. (d) Iridium mass based OER activities for IrOOH<sub>x</sub>/TiO<sub>2</sub> based catalysts determined by cyclic voltammetry measurements (1<sup>st</sup> and 20<sup>th</sup> cycle each) of respective catalyst samples (15 μg<sub>Ir</sub> abs.) on fluorine doped tin oxide substrates.

To assess the electrocatalytic activity of the oxidized IrOOH<sub>x</sub>/TiO<sub>2</sub> and the IrO<sub>2</sub>/TiO<sub>2</sub> reference catalyst (Elyst Ir75, UMICORE), cyclic voltammetry in a potential window up to 1.8 V vs. RHE was conducted on fluorine doped tin oxide substrates at room temperature with results presented in Figure 4d, S7, S8 and **Figure S12**. Figure 4d shows a visibly increased activity of the 375 °C oxidized sample compared to the non-heated 30 wt% Ir

containing IrOOH<sub>x</sub>/TiO<sub>2</sub> with increasing overpotential, which can be explained by the significantly higher conductivity of the oxidized sample and thus a reduced ohmic resistance at high current densities. The contrasting example is given by the 400 °C oxidized sample (Figure 4d), showing only a low OER activity due to its limited conductivity (Figure 1).

The 45 wt% sample series shows an even higher spread in OER activity (Figure S7) with increasing overpotential, which is in agreement with the larger change in conductivity upon oxidation (Figure 1). Due to the retained conductivity, the 400 °C oxidized sample thereby still shows a moderate OER activity compared to the 30 wt% Ir sample.

Absolute OER activities normalized to the iridium mass are very similar for the 30 and 45 wt% Ir containing IrOOH<sub>x</sub>/TiO<sub>2</sub> catalysts oxidized at 375 °C, which is regarded to be the optimum synthesis temperature resulting in maximized conductivity and activity for the 30 wt% sample series (Figure S12). In the low overpotential range of 300 mV, the 375 °C oxidized 30 and 45 wt% IrOOH<sub>x</sub>/TiO<sub>2</sub> catalysts exhibit an Ir-based OER current of about 62 and 71A g<sub>Ir</sub><sup>-1</sup> after the 10<sup>th</sup> cycle, respectively, which is about 8 times higher than the measured 8 A g<sub>Ir</sub><sup>-1</sup> of the 75 wt% Ir containing IrO<sub>2</sub>/TiO<sub>2</sub> reference catalyst under the same conditions. At an elevated overpotential of 420 mV, the 30 and 45 wt% Ir coated catalysts show a coinciding activity of about 1048 and 1047 A g<sub>Ir</sub><sup>-1</sup>, respectively, which is still 3 times higher than the measured 345 A g<sub>Ir</sub><sup>-1</sup> of the reference catalyst.

Comparison to literature shows a similar high activity of our prepared catalysts to a very high surface area (245 m<sup>2</sup> g<sup>-1</sup>) 40 mol% Ir ( $\triangleq$  56 wt% Ir) containing IrO<sub>2</sub>/TiO<sub>2</sub> catalyst prepared by Oakton *et al.*, which delivers 70 A g<sup>-1</sup> at an overpotential of 287 mV.<sup>[50]</sup> However, the reported conductivity of the randomly mixed oxide of 0.26 S cm<sup>-1</sup> is expected to limit the performance in the high overpotential range that is typically used for the operation of an electrolyzer. Compared to the highly active catalyst reported by Hu *et al.* with 548 A g<sub>Ir</sub><sup>-1</sup> at an overpotential of 362 mV (26 wt% Ir containing Nb-doped TiO<sub>2</sub> supported IrO<sub>2</sub>

nanoparticle catalyst), our 30 wt% Ir containing IrOOH<sub>x</sub>/TiO<sub>2</sub> catalyst oxidized at 375 °C shows a slightly lower mass-based activity of 487 A g<sub>Ir</sub><sup>-1</sup> determined at the same overpotential.<sup>[54]</sup>

Although the supported catalysts presented here do not surpass the best performing NTO supported IrO<sub>2</sub> nanoparticle catalyst at moderate current densities, they combine required key properties of an OER catalyst that can effectively reduce the Ir-loading in the anode layer of an actual PEM electrolyzer such as high conductivity, high iridium dispersion and resulting low Ir-density with a high catalytic activity.<sup>[5, 62]</sup>

The beneficial effect of the controllable oxidation of a thin  $IrOOH_x$  layer on the  $TiO_2$  support is further supported by comparison with an unsupported  $IrO_x$  nanoparticle reference catalyst. This was obtained by oxidation of an  $IrCl_3xH_2O$  precursor in molten  $NaNO_3$  at 375 °C with resulting particle sizes of ~2 nm and a crystallinity comparable to that of the  $IrO_x$  phase of the  $TiO_2$ -supported catalysts. (**Figure S10**). Chronopotentiometry measurements (**Figure S11**) reveal that the unsupported  $IrO_x$  electrode shows a very similar potential of ~1.58 V vs. RHE as the 30 and 45 wt% Ir containing  $TiO_2$ -supported catalysts, which feature a significantly lower iridium density.

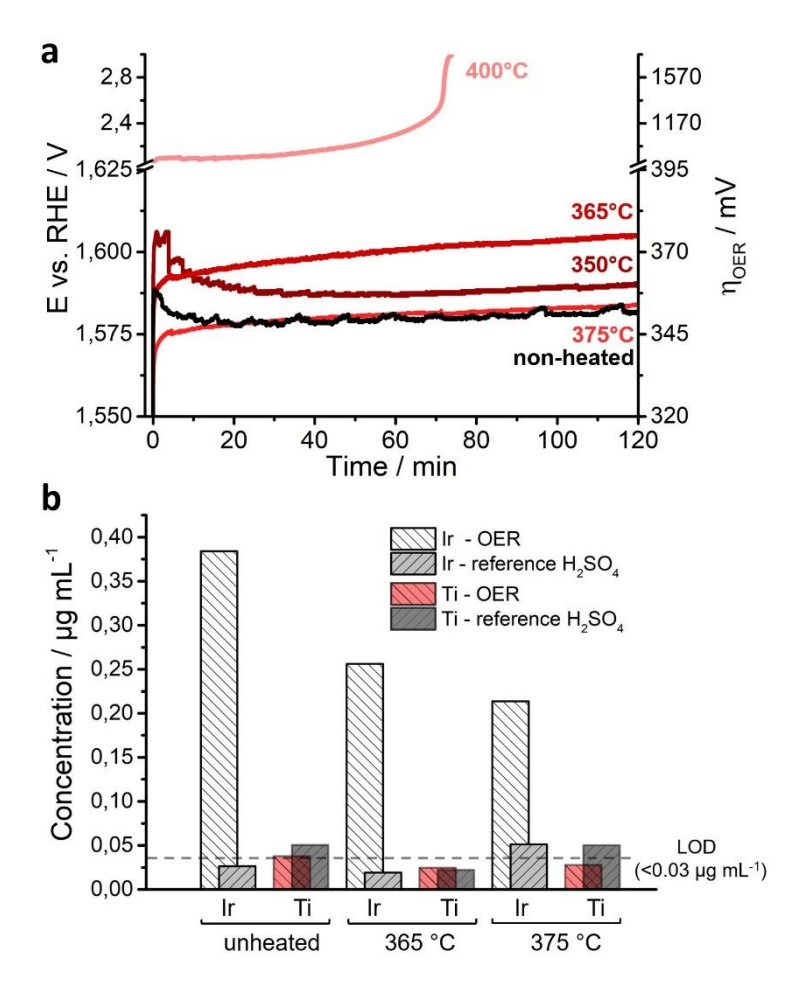


**Figure 5.** Stability and activity measurements by chronopotentiometry and detection of dissolved iridium by ICP-OES of 30 wt% Ir containing TiO<sub>2</sub> supported catalyst. Chronopotentiometry measurements (a) at  $j = 10 \text{ mA cm}^{-2}$  over 120 min. ICP-OES measurements of dissolved Ir and Ti during 24 h of chronopotentiometry at  $j = 50 \text{ mA cm}^{-2}$  (white and red bars; declining dash) or storage in the acidic electrolyte without applied potential (grey bars; rising dash) for non-heated, 365 °C and 375 °C oxidized catalyst.

A further important requirement for the use of the  $IrO_x$ ,  $IrO_2/TiO_2$  as catalyst in electrolyzers is their stability under OER conditions. This aspect was initially investigated by means of chronopotentiometry measurements over 2 h that were conducted at a moderate current density of 10 mA cm<sup>-2</sup> as depicted in **Figure 5**a for the 30 wt% Ir containing catalyst. Nonheated (black curve) as well as 350 °C oxidized  $IrOOH_x/TiO_2$  catalyst (dark red curve) thereby show the characteristic potential evolution of metallic or hydrous  $IrO_x$  with a decrease in the potential over an activation period of about 30 min and a slight increase of the

potential over the remaining measurement period. However, the curve of the 350 °C oxidized sample is shifted about 10 mV to higher potentials indicating a slightly decreased activity.

Increasing the oxidation temperature to 365 °C leads to a dehydration of the IrOOH<sub>x</sub> phase and formation of IrO<sub>x</sub> particles, which already resemble the oxide in its potential course over time but with a reduced activity attributed to mass transfer limitations caused by dehydration as proposed by *Geiger et al.*.<sup>[64]</sup> As shown by RDE and cyclic voltammetry (Figure 4b,d and S8c), oxidation at 375 °C results in an optimum in catalytic activity reflected by a potential curve decreased by about 21 mV compared to the 365 °C sample and coinciding with the non-heated IrOOH<sub>x</sub>/TiO<sub>2</sub> at a potential of 1.58 V vs. RHE after 2 h. The drastic reduction in conductivity and formation of rather isolated rutile IrO<sub>2</sub> crystals upon oxidation at 400 °C leads to significantly decreased OER activity, reflected by a required potential of 2.1 V vs. RHE in the chronopotentiometry with a complete loss of activity after 75 min.

The higher-loaded 45 wt% Ir containing catalyst series exhibits a similar trend shown in **Figure S13**a, although the potential curve of the 350 °C oxidized IrOOH<sub>x</sub>/TiO<sub>2</sub> already resembles that of an Ir oxide. Oxidation at 400 °C again leads to a significant reduction of the OER activity reflected by an initial potential of 1.72 V vs. RHE that constantly rises to over 2.8 V vs. RHE within the measurement period. The chronopotentiometry results are in accordance with the RDE and CV data and confirm the formation of a highly active amorphous oxidic iridium phase in the temperature range of 365 - 375 °C that exhibits a similar OER activity as the initial hydrous IrOOH<sub>x</sub> and which is stable under OER conditions over the measurement period.

According to literature, oxidation (e.g., thermal annealing) of hydrous iridium oxide films (HIROF) is a known and well-investigated technique to enhance the corrosion stability under OER conditions, required for a stable operation as PEM anode catalyst. [64-66]

To quantify the stability of the oxidized IrOOH<sub>x</sub>/TiO<sub>2</sub> catalysts, inductively coupled plasma optical emission spectroscopy (ICP-OES) of dissolved iridium in the electrolyte was performed after 24 h of electrolysis (Figure 5b and Figure S13, corresponding chronopotentiometry data **Figure S14-15**) with 1 cm<sup>2</sup> electrodes at a current density of 50 mA cm<sup>-2</sup>. The Ir concentration is shown to be inversely correlated to the oxidation temperature starting with 38  $\mu$ g<sub>Ir</sub> mL<sup>-1</sup> in 24 h for the non-heated 30 wt% Ir containing hydrous oxide and significantly declining to 26  $\mu$ g<sub>Ir</sub> mL<sup>-1</sup> for the 365 °C oxidized sample down to 21  $\mu$ g<sub>Ir</sub> mL<sup>-1</sup> for IrOOH<sub>x</sub> oxidized at 375 °C.

These findings are at first sight in contrast to literature reports about the stability and activity of hydrous iridium oxide and a suggested compromise by tuning the crystallinity with the annealing temperature. [12, 64] In general, thermal annealing was shown to decrease the activity with increasing temperature for several iridium based systems, which is explained by a change in the oxide stoichiometry, a lower amount of accessible active sites and mass transfer limitations due to dehydration in the lower temperature regime. [32, 35, 60, 66, 90]

For our oxidized IrOOH<sub>x</sub>/TiO<sub>2</sub> catalysts a reduction of the electrochemical surface area is qualitatively indicated by cyclovoltammetry (Figure 4, S9), but it is regarded to be also accompanied by an increase in the catalyst surface area by the formation of small nanoparticles from an amorphous IrOOH<sub>x</sub> phase. These findings can be explained by the transition of a bulk to a surface redox active catalyst and do not necessarily imply a lower activity if the surface to bulk ratio of iridium active phase is high enough.<sup>[89]</sup>

Based on the data presented in this work, we therefore conclude that for the thin intermediate  $IrO_x$  phase no trade-off exists between catalytic activity and stability with respect to the hydrous  $IrOOH_x$ , which further outlines the advantage of the proposed synthesis method in addition to the established positive effects of the increased conductivity and enhanced morphology.

### 2.3 Electrochemical characterization of membrane electrode assemblies (MEA)

To investigate the catalytic performance and potential application of the oxidized OER catalyst at industrially relevant current densities in a PEM electrolyzer membrane electrode assembly (MEA) measurements with 5 cm<sup>2</sup> active area were conducted at 80 °C (see experimental section for further details).

Following the concept of a reduction of the iridium loading, the untreated and oxidized IrOOH<sub>x</sub>/TiO<sub>2</sub> catalysts were applied at low areal loadings of 0.24 and 0.34 mg<sub>Ir</sub> cm<sup>-2</sup>, respectively, and compared to a TiO<sub>2</sub>/IrO<sub>2</sub> industrial reference catalyst (Elyst Ir75, UMICORE) with 75 wt% Ir at a loading of 1.25 mg<sub>Ir</sub> cm<sup>-2</sup> (**Figure 6**). The areal loading of the reference catalyst can thereby not be significantly lowered beyond this value without drastically decreasing the performance due to its morphology and the resulting discontinuity of the electrode layer, which is the main motivation for the development of novel nanostructured TiO<sub>2</sub> supported catalysts with low packing density.<sup>[90]</sup>

In contrast to the liquid cell measurements at low current densities shown in Figure 4 and 5, in the MEA the non-oxidized 45 wt% Ir containing IrOOH<sub>x</sub>/TiO<sub>2</sub> catalyst exhibits a poor performance with a steep rise of the potential reaching a cell voltage of over 2.5 V around only  $\approx 0.5$  A cm<sup>-2</sup>. The low catalytic activity can be explained by a comparably low conductivity already indicated by powder pellet measurements (Figure 1d) which also did not allow a determination of the high frequency resistance of the MEA. This emphasizes the importance of high electrical conductivity of the catalyst material which becomes decisive at elevated and high current densities.

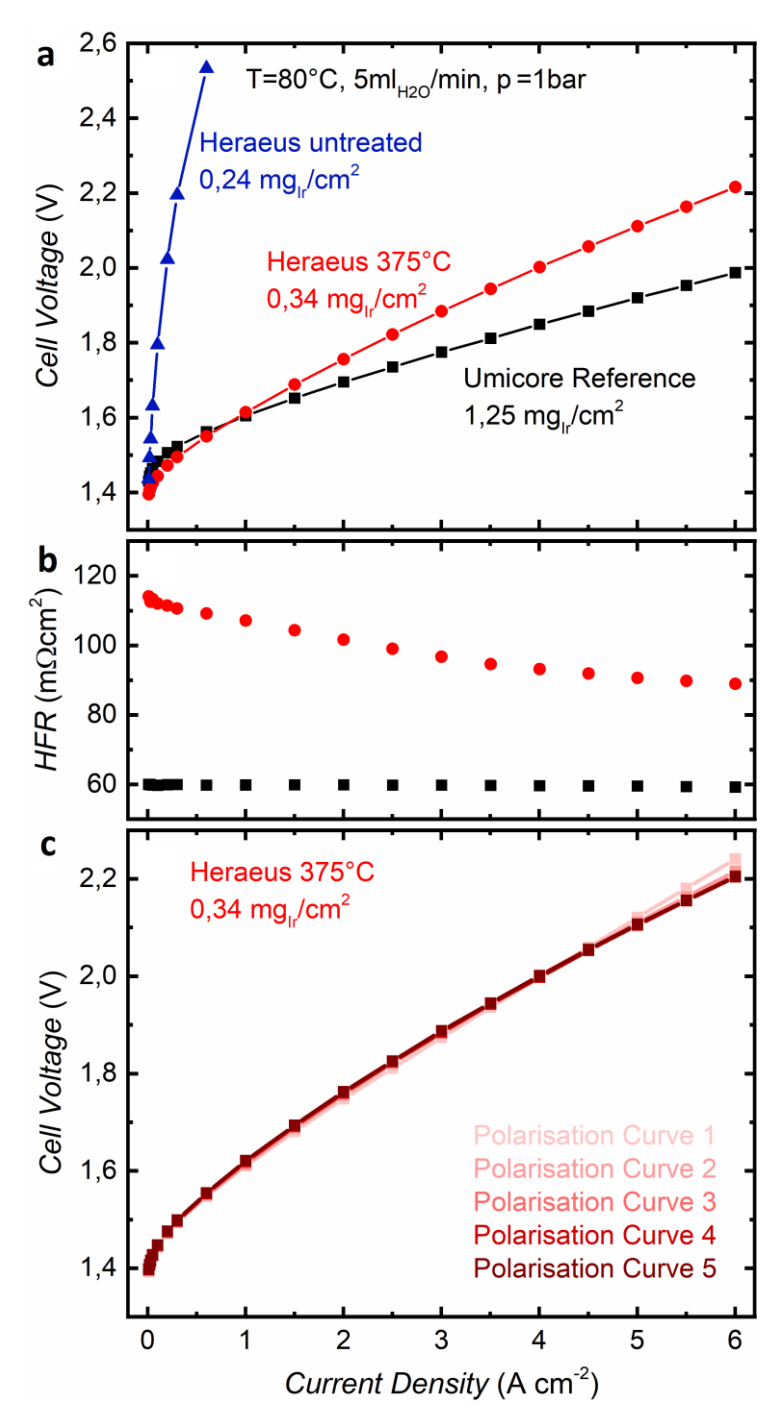


**Figure 6.** Membrane electrode assembly (MEA) measurements of oxidized 45 wt% Ir containing TiO<sub>2</sub> / IrO<sub>2</sub> catalyst. (a) Polarization curves (1<sup>st</sup> scan cycle) of non-oxidized (blue curve) and 375 °C oxidized (red curve) TiO<sub>2</sub>/IrO<sub>2</sub> catalyst with low membrane loadings (0.24-0.34 mg<sub>Ir</sub> cm<sup>-2</sup>) versus an industrial benchmark catalyst (black curve, UMICORE reference Elyst Ir75) with 75 wt% Ir content and Ir loading of 1.25 mg<sub>Ir</sub> cm<sup>-2</sup>. (b) High frequency resistance of 375 °C oxidized (red data points) TiO<sub>2</sub>/IrO<sub>2</sub> catalyst and industrial benchmark catalyst (black data points). (c) Five consecutive polarization curves of TiO<sub>2</sub>/IrO<sub>2</sub> catalyst with 45 wt% Ir loading oxidized at 375 °C.

The 45 wt% Ir containing catalyst oxidized at 375 °C in molten NaNO<sub>3</sub> with its significantly improved conductivity outperforms the 75 wt% Ir containing reference catalyst with its  $\approx$ 3.7 times higher iridium loading on the membrane at current densities of up to  $\approx$ 1 A cm<sup>-2</sup>. At even higher current densities of up to 6 A cm<sup>-2</sup>, the cell voltage rises up to 2.2 V versus 2.0 V determined for the reference catalyst. The higher performance at current densities >1 A cm<sup>-2</sup> of the less electrochemically active reference catalyst (Figure 6, S9) can be explained by its high electrical conductivity (measured in powder form) of  $\approx$ 73 S cm<sup>-1</sup> (vs.  $\approx$ 40 S cm<sup>-1</sup> for the 45 wt% Ir catalyst oxidized at 375 °C) confirmed by impedance spectroscopy (Figure 6b) with a high frequency resistance (HFR) of 60 m $\Omega$ cm<sup>2</sup> compared to 115-90 m $\Omega$ cm<sup>2</sup> for the 45 wt% Ir catalyst oxidized at 375 °C. For a more detailed investigation of the influence of the electrical conductivity of the catalyst on the MEA performance we refer to the study of Bernt *et al* ..<sup>[91]</sup>

A first stability assessment of the 45 wt% Ir containing 375 °C oxidized catalyst was performed by recording five consecutive polarization curves up to 6 A cm<sup>-2</sup> (Figure 6c) which mostly overlap and therefore do not reveal a significant degradation, as already indicated by chronopotentiometry measurements at lower current densities (Figure S9, S13).

The 30 wt% Ir containing catalyst introduced in this work was also characterized by MEA measurements with loadings of 0.12-0.65 mg<sub>Ir</sub> cm<sup>-2</sup> (**Figure S16**), again showing a significantly decreased cell voltage for the oxidized samples. However, all samples of this series exhibited a lower electrochemical performance than the reference catalyst at current densities above  $\approx$ 250 mA cm<sup>-2</sup>. The discrepancy of a high catalytic activity at low current densities (Figure 4, S12) and a lower OER performance in the MEA compared to the 45 wt% Ir sample as well as the reference catalyst, at industrially relevant current densities of several A cm<sup>-2</sup>, can be explained by the lower maximum conductivity of  $\approx$ 11 S cm<sup>-1</sup> determined for the active material that leads to high voltage losses in the electrolysis cell. In addition, an

increasing cell voltage within five consecutive scan cycles of the 30 wt% Ir containing catalyst oxidized at 365°C (Figure S16b) may indicate a catalyst degradation but would need further analysis for a detailed understanding of the electrochemical behavior of this catalyst sample.

Considering the newly introduced catalyst synthesis, nanomorphology and OER performance at low and high current densities, undoped titania with a moderately high surface area and low powder density of  $\approx 0.1-0.2$  g cm<sup>-3</sup> therefore presents a suitable corrosion-resistant support material for the synthesis of novel highly active OER catalysts with low Ir-density. Neglecting the influence of the 1–2 nm thin coating layer on the TiO<sub>2</sub> mass, the 30 wt% Ir containing IrOOH<sub>x</sub>/TiO<sub>2</sub> catalyst series exhibits a calculated Ir density as low as 0.046 – 0.083 g<sub>Ir</sub> cm<sup>-3</sup> in the dry powder.

The 45 wt% Ir containing titania supported catalyst series features calculated Ir densities in the non-compressed catalyst powder between  $0.095-0.17~g_{Ir}~cm^{-3}$  that still represent a major advance towards the reduction of the noble metal content in electrolyzer anodes when comparing to the experimentally determined Ir density (bulk powder density) of  $\approx 1.5~g_{Ir}~cm^{-3}$  [36] for the industrial IrO<sub>2</sub>/TiO<sub>2</sub> reference catalyst with 75 wt% Ir loading.

### 3. Conclusion

In this work, the facile synthesis of a novel highly active and industrially applicable IrO<sub>2</sub> nanoparticle based TiO<sub>2</sub> supported OER catalyst for PEM electrolysis is presented. IrOOH<sub>x</sub>/TiO<sub>2</sub> OER catalyst with nominal homogeneous loadings of 30 and 45 wt% Ir were used a precursor phase. By employing oxidation in molten NaNO<sub>3</sub>, the moderately conductive IrOOH<sub>x</sub> phase (3 and 0.2 S cm<sup>-1</sup> for 30 and 45 wt% Ir containing catalyst, respectively) could be transformed to small intergrown IrO<sub>x</sub>/IrO<sub>2</sub> nanoparticles on the nonconductive TiO<sub>2</sub>. This way, the conductivity of the TiO<sub>2</sub>-supported catalysts reached values as high as 11 and 40 S cm<sup>-1</sup> for the 30 and 45 wt% Ir containing catalyst, respectively, at the

temperature optimum for oxidation of 375 °C. In-depth structural characterization shows that a higher oxidation temperature of 400 °C leads to further particle growth consuming surrounding  $IrOOH_x$  and  $IrO_x$  particles, which causes the formation of isolated or poorly interconnected rod-like  $IrO_2$  particles of about 10 and up to 100 nm length for the 30 and 45 wt% Ir catalysts, respectively.

Electrochemical characterization in liquid cells revealed an Ir mass-based OER activity exceeding an industrial IrO<sub>2</sub>/TiO<sub>2</sub> reference catalyst (Elyst Ir75, UMICORE) with 75 wt% Ir by a factor of 3 and 8 in the moderate and low overpotential regimes of 420 and 300 mV, respectively. The 30 wt% Ir containing IrOOH<sub>x</sub>/TiO<sub>2</sub> catalyst oxidized at 375 °C in molten NaNO<sub>3</sub> thereby delivers 62 A g<sub>Ir</sub><sup>-1</sup> at  $\eta_{OER}$ =300 mV and 572 A g<sub>Ir</sub><sup>-1</sup> at  $\eta_{OER}$ =380 mV, which is in the range of best performing IrO<sub>2</sub> nanoparticle OER catalysts with Nb-doped TiO<sub>2</sub> support. Intermediate term chronopotentiometry measurements over 24 h and ICP-OES measurements of dissolved Ir in the electrolyte further confirm a significantly increased stability of the IrOOH<sub>x</sub>/TiO<sub>2</sub> catalyst upon oxidation in molten salt at the temperature optimum of 375 °C. Concerning the relevance of the introduced oxidation procedure for PEM electrolysis, MEA measurements further establish the significantly increased performance of the IrOOH<sub>x</sub>/TiO<sub>2</sub> catalyst upon oxidation that even outperformed a state-of-the art TiO<sub>2</sub>/IrO<sub>2</sub> reference catalyst with 3.6 times the areal iridium loading in a range of up to 1 A cm<sup>-2</sup>. For a further improvement of the electrocatalytic activity at high current densities, the electrical conductivity of the catalyst should be further increased (above 40 S cm<sup>-2</sup> determined for the best performing oxidized 45 wt% Ir containing sample), which is regarded to be possible by optimizing the support nanomorphology, support surface area as well as the IrO2 layer thickness and crystallinity.

Overall, our synthesis approach enables the fabrication of a novel supported OER catalyst powder with greatly reduced Ir-density of 0.046 - 0.083 g<sub>Ir</sub> cm<sup>-3</sup> (30 wt% Ir catalyst) through

the homogeneously coated TiO<sub>2</sub> nanostructure and retained catalytic activity, which allows a significant reduction of the noble metal content in anodes of PEM electrolyzes. Importantly, the general findings of our work are not specifically limited to the TiO<sub>2</sub> support employed here, but rather demonstrate that the controlled crystallization of amorphous IrOOH<sub>x</sub> to a crystalline and interconnected IrO<sub>2</sub> particle layer enables the significant reduction in Ir loading by maintaining high catalytic activity and stability. Provided the required wetting can be ensured, our novel approach is universally applicable to any type of support, and it can be expected that even further reduction of the iridium density with enhanced OER activity could be achieved by the use of more advanced oxidic support morphologies such as microparticles with inverse opal structure recently demonstrated by our group, or highly conductive and corrosion-stable TiON phases obtained by Bele *et al.*.<sup>[36, 56]</sup>

## 4. Experimental

## 4.1 TiO<sub>2</sub>/IrOOH<sub>x</sub> precursor phase

Two batches of IrOOH<sub>x</sub> coated  $TiO_2$  catalyst were obtained from HERAEUS Deutschland GmbH & Co. KG with nominal Ir metal contents of  $\approx 30$  and 45 wt% Ir, respectively. The catalyst provided consists of a fine, non-agglomerated powder and was used as received for further experiments.

# 4.2 Synthesis of TiO2 supported IrOx and IrO2 nanoparticles and unsupported IrOx

The synthesis of IrO<sub>x</sub> and IrO<sub>2</sub> nanoparticles supported by TiO<sub>2</sub> from an amorphous IrOOH<sub>x</sub> precursor phase is based on the well-known molten salt oxidation route in NaNO<sub>3</sub>, initially introduced in 1923 by Adams and Shriner for the preparation of platinum oxide nanoparticles and described by Oakton *et al.* for the preparation of a TiO<sub>2</sub>/IrO<sub>2</sub> OER catalyst from a mixture of molecular precursors.<sup>[50, 92]</sup> The process was adapted to transform a thin amorphous IrOOH<sub>x</sub> layer on the TiO<sub>2</sub> substrate to IrO<sub>x</sub> nanoparticles.

30 or 45 wt% Ir  $TiO_2/IrOOH_x$  powder and  $NaNO_3$  (VWR,  $\geq 99.9\%$ ) were mixed in a mass ratio of 1:12 with an addition of 24 mass equivalents of deionized  $H_2O$ . In a typical reaction

500 mg of TiO<sub>2</sub>/IrOOH<sub>x</sub> catalyst were added to 6.0 g of NaNO<sub>3</sub> with the addition of 12 mL H<sub>2</sub>O. The reaction mixture was stirred and sonicated 3 times for 20 min for a complete dissolution and intermixing of the precursors. In a following step the reaction mixture was dried in glass dishes by evaporation on a hot plate at 95 °C to obtain a greyish/white product that was transferred to a ceramic calcination tray and placed in a laboratory oven (NABERTHERM, model N15/65SHA). All reactions were first heated to 150 °C for 2 h (3 °C min<sup>-1</sup> heating ramp) in air to remove residual water in the reaction mixture. Depending on the targeted crystallinity of the IrO<sub>x</sub>, the product was further heated to a temperature between 350 and 400 °C for 1 h (3 °C min<sup>-1</sup> heating ramp) in air. The resulting TiO<sub>2</sub>/IrO<sub>x</sub> was encapsulated in the NaNO<sub>3</sub> melt after cool down and isolated by 4 consecutive washing steps with DI H<sub>2</sub>O and centrifugation. To obtain a fine powder, the product was finally freeze-dried using an ALPHA 1-4 machine (MARTIN CHRIST GEFRIERTROCKNUNGSANLAGEN GMBH).

The synthesis of the unsupported IrO<sub>x</sub> reference was performed as described above but with IrCl<sub>3</sub>xH<sub>2</sub>O (SIGMA-ALDRICH, reagent grade) as IrO<sub>x</sub> precursor. The unsupported reference sample was oxidized at 375 °C in NaNO<sub>3</sub>.

# 4.3 Physico-chemical characterization

Wide angle X-ray diffraction (XRD) analysis was carried out in transmission mode using a STOE STADI P diffractometer with Cu  $K_{\alpha 1}$  radiation ( $\lambda = 1.54060$  Å) and a Ge(111) single crystal monochromator equipped with a DECTRIS solid state strip detector Mythen 1K. Powder XRD patterns of the samples were collected with an omega-2theta scan in the  $2\theta$  range from 5° to 90° with a step size of 1° and fixed integration time of 25 – 35 seconds per step and a resolution of 0.05°. The size of crystalline domains of IrO<sub>2</sub>, TiO<sub>2</sub> (anatase phase) and TiO<sub>2</sub> (rutile phase) nanoparticles were calculated with Scherrer's Equation from line broadening of the 101, 101 and 110 reflections, respectively. Reflection positions were

compared to XRD reference patterns for the IrO<sub>2</sub> phase (ICDD card #00-015-0870, tetragonal symmetry, a = b = 4.4983 Å, c = 3.1544 Å,  $\alpha = \beta = \gamma = 90^{\circ}$ ), TiO<sub>2</sub> (anatase) (ICDD card #00-004-0477, tetragonal symmetry, a = b = 3.783 Å, c = 9.510 Å,  $\alpha = \beta = \gamma = 90^{\circ}$ ) and TiO<sub>2</sub> (rutile) (ICDD card #00-004-0551, tetragonal symmetry. a = b = 4.594 Å, c = 2.958 Å,  $\alpha = \beta = \gamma = 90^{\circ}$ ).

Raman spectroscopy was carried out using a LabRAM HR UV-Vis (HORIBA JOBIN YVON) Raman Microscope (OLYMPUS BX41) with a SYMPHONY CCD detection system and a He-Ne laser ( $\lambda = 633$  nm). Spectra were recorded using a lens with a 10-fold magnification in the range from 100 cm<sup>-1</sup> to 1000 cm<sup>-1</sup> with filters of OD 0.3 - 0.6. Spectrum accumulation mode was used with integration times of 30 sec per spectrum and 600 cycles. The data acquisition was carried out with LabSpec software.

HRTEM, HAADF-STEM images were recorded using a FEI Titan Themis 80-300 microscope with aberration correction of the probe-forming lenses operated at 120 kV or 300 kV, respectively. Energy dispersive X-ray spectroscopy (EDX) was performed using a SuperX windowless, four quadrant Silicon drift detector with a solid angle of 0.7 sr. TEM specimens were prepared from nanoparticles in a 1:1 (v/v) ratio of water to ethanol and deposited on a carbon-film coated copper grid and dried in air.

Scanning electron microscopy (SEM) images were recorded with a FEI Helios Nanolab G3 UC scanning electron microscope equipped with a field emission gun operated at 3 – 5 kV. Specimens were prepared from powders in a 1:1 (v/v) ratio of water to ethanol and deposited on FTO or Si substrates that were glued onto a stainless-steel sample holder with silver lacquer. EDX measurements were performed at an operating voltage of 20 kV with a X-Max<sup>N</sup> Silicon Drift Detector with 80 mm<sup>2</sup> detector area (OXFORD INSTRUMENTS) and AZTec acquisition software (OXFORD INSTRUMENTS).

Conductivity measurements of TiO<sub>2</sub> supported IrOOH<sub>x</sub> and the IrO<sub>2</sub>/TiO<sub>2</sub> reference catalyst (Elyst Ir75, UMICORE) were carried out on a HMS 3000 apparatus (ECOPIA) in the Vander-Pauw geometry (5 mm separation of electrodes). Powder samples were measured as pellets that were compressed for 10 min at 150 kg cm<sup>-2</sup>. Due to restrictions on sample volume conductivity measurements of TiO<sub>2</sub>/IrO<sub>2</sub> (45 wt% Ir, 400 °C oxidation) were conducted on an in-house constructed dc-conductivity measurements cell on loosely compressed powders by recording *I-V* curves between -5 to +5 V with an AUTOLAB 302N potentiostat/galvanostat (METROHM AUTOLAB B.V.).

Thermogravimetric analysis (TGA) and differential scanning calorimetry (DSC) of the samples was performed on a NETZSCH STA 440 C TG/DSC (heating rate of 10 K min<sup>-1</sup> in a stream of synthetic air of about 25 mL min<sup>-1</sup>).

Stability measurements of the IrOOH<sub>x</sub>, IrO<sub>x</sub> and IrO<sub>2</sub> coated TiO<sub>2</sub> electrodes with an absolute loading of 400 µg<sub>catalyst</sub> were performed by analyzing electrolyte (0.5 M H<sub>2</sub>SO<sub>4</sub>) aliquots (1.0 mL of 20.0 mL total volume) by inductively coupled plasma optical emission spectrometry after chronopotentiometry measurements over 24 h at a current density of 6.67 mA cm<sup>-2</sup> (10 mA absolute). Reference samples were stored in electrolyte under the same conditions for 24 h without applying a potential. All samples were stored/washed in electrolyte (which was discarded) for 5 min prior to each measurement to detect only potential/current induced dissolution related to electrolysis and avoid detection of dissolved ions from initial contact with the acidic electrolyte.

## 4.4 Electrochemical characterization by RDE and liquid cell measurements

All electrochemical measurements at room temperature were carried out in a 3-electrode setup with quartz cells filled with 20 mL 0.5 M H<sub>2</sub>SO<sub>4</sub> (SIGMA-ALDRICH, Titripur® volumetric standard) as electrolyte using an PGSTAT302N potentiostat/galvanostat (METROHM AUTOLAB B.V.) equipped with a FRA32 M impedance analyzer connected to

a Hydroflex reversible hydrogen electrode (GASKATEL Gesellschaft für Gassysteme durch Katalyse und Elektrochemie mbH) or Hg/HgSO<sub>4</sub>/K<sub>2</sub>SO<sub>4</sub>(sat.) (REF601, RADIOMETER ANALYTICAL-HACH COMPANY) for cyclic voltammetry and chronopotentiometry measurements, respectively.

The electrochemical activity of the catalysts on FTO substrates was measured by iR-drop corrected linear sweep voltammetry (LSV) in a potential window of 1.0 – 1.8 V vs. RHE in 20 scan cycles with a scan rate of 20 mV s<sup>-1</sup>. Impedance spectroscopy data at 0.5 V vs. RHE was recorded prior to each measurement to determine the corresponding electrolyte resistance (95 %) from the high frequency region ( $R_s$  determined from semi-circle or linear fit). The iridium mass-based catalyst activity in A  $g_{Ir}^{-1}$  was calculated from the coating volume (3 -15 μl) of a dispersion of known concentration (2 mg<sub>catalyst</sub> ml<sup>-1</sup>) to deposit 15 μg<sub>Ir</sub> on each electrode on a masked area of 0.196 cm<sup>-2</sup>. The coating volume for the 30 and 45 wt% Ir (nominal loading values) containing IrOOH<sub>x</sub>/TiO<sub>2</sub> catalysts were calculated according to Ir content measured by SEM/EDX of 28 and 52 wt% respectively from the obtained batches (see Table S1-5 for details). The difference of the local Ir loading to the stated nominal values obtained by elemental analysis can be explained by a certain inhomogeneity resulting from the industrial-type kilogram scale synthesis method of the catalyst. A further explanation for the deviation might be the employed EDX quantification system and its software with its implemented structural model which is not specified for nanometer-sized core-shell morphologies. Current densities were determined from the mean value of capacity current corrected (mean current in potential region 1.0 – 1.23 V vs. RHE) anodic and cathodic scans of the respective LSV cycle.

Stability measurements of electrodes were performed with an  $Hg/HgSO_4/K_2SO_4(sat.)$  reference electrode. Potentials versus the reversible hydrogen electrode  $E_{RHE}$  were calculated by measuring the open circuit potential of the  $Hg/HgSO_4/K_2SO_4(sat.)$  reference electrode

against a Hydroflex reversible hydrogen electrode (GASKATEL Gesellschaft für Gassysteme durch Katalyse und Elektrochemie mbH) before and after each chronopotentiometry measurement and by shifting the measured potential accordingly.

For the stability measurements including ICP-OES analysis of the electrolyte, chronopotentiometry measurements with electrodes of 1 cm<sup>2</sup> active area and a total coating of 200 μg<sub>Ir</sub> were prepared. Prior to each 24 h measurement at a current density of 50 mA cm<sup>-2</sup> electrodes were immersed in fresh electrolyte for 1 min that was afterwards discarded to wash away unattached particles from the electrode surface. Electrolysis was performed with 20 mL of fresh electrolyte from which 2 mL were taken for ICP-OES analysis. Rotating disk electrode (RDE) measurements were conducted with a MSR Electrode rotator with mirror finished polished 5 mm diameter glassy carbon disc insets (PINE RESEARCH INSTRUMENTATION) connected to an Autolab PGSTAT302N potentiostat/galvanostat equipped with a FRA32 M impedance analyzer (METROHM AUTOLAB B.V.) and a double-walled glass cell with Luggin-capillary for the reference electrode compartment. Electrolyte temperature of 60.0±0.1 °C was maintained by a KISS 104A circulation thermostat (PETER HUBER KÄLTEMASCHINENBAU AG) and monitored with an immersed Kelement temperature sensor. The Nernst potential for water oxidation was kept constant by continuous O<sub>2</sub> (AIR LIQUIDE, AlphaGaz® 2 N5 purity) purging of the electrolyte (0.5 M H<sub>2</sub>SO<sub>4</sub>, SIGMA-ALDRICH, Titripur® volumetric standard). Catalyst loadings of 50 μg<sub>Ir</sub> cm<sup>-2</sup> (10 μg<sub>Ir</sub> absolute) were drop-casted on cleaned glassy carbon discs and dried at 60 °C before applying 10 µL of a 1:100 dilution of a Nafion® perfluorinated resin solution (SIGMA-ALDRICH, 5 wt% in lower aliphatic alcohols and water (15-20% water) in a H<sub>2</sub>O/*i*PrOH mixture (1:1 v/v). The electrolyte resistance was determined before and after each RDE measurement in the high frequency region of recorded impedance spectra at 0.5 V vs. RHE. Due to low current densities reached in the measurement protocol and repeatedly low

electrolyte resistance values around 5 – 10  $\Omega$ , an iR drop correction of the recorded data was not performed. The applied measurement protocol consisted of 75 LSV cycles starting from 1.0 V vs. Hydroflex RHE (GASKATEL Gesellschaft für Gassysteme durch Katalyse und Elektrochemie mbH). The upper vertex potential was defined to be at a current density of  $j = 1 \text{ mA cm}^{-2}$  ( $i_{abs} = 0.2 \text{ mA}$ ,  $A = 0.196 \text{ cm}^2$ ). Reported current densities were determined from the mean value of capacity current (mean value in potential region 1.0 - 1.23 V vs. RHE) corrected anodic and cathode scan for a given overpotential  $\eta_{OER}$  of the respective scan cycle.

Additional cyclic voltammetry measurements over the potential range of 0.05 – 1.52 V vs. RHE were performed during RDE measurements to identify redox features and compare the electrocatalytically active surface area of catalyst samples. Three cyclic voltammograms were therefore recorded prior to each RDE measurement (as described above), after 50 and after 75 RDE LSV cycles.

## 4.5 Membrane electrode assembly (MEA) preparation and cell assembly

MEAs with an active area of 5 cm<sup>2</sup> were prepared by using a decal transfer method. The electrodes for the hydrogen evolution reaction on the cathode were prepared from platinum supported on Vulcan XC72 carbon with a metal loading of 45.8 wt% (TEC10V50E, TANAKA, Japan). For the oxygen evolution reaction on the anode, crystalline c-IrO<sub>2</sub>/TiO<sub>2</sub> (Elyst Ir75 0480, UMICORE, Germany) with 75 wt% Ir or amorphous a-IrO(OH)<sub>x</sub>/TiO<sub>2</sub> with 30wt% or 45 wt% Ir (HERAEUS Deutschland GmbH & Co. KG, Germany) as well as oxidized samples described in this work were used. The inks were prepared from catalyst powder, 2-propanol (purity  $\geq$  99.9%, from SIGMA-ALDRICH), and Nafion® ionomer solution (SGE-10-0ICS, 20 wt% ionomer, D2021 from DUPONT, USA). 5 mm ZrO<sub>2</sub> grinding beads were added and the ink was mixed for at least 18 h on a roller mill (from

RATEK, Australia). The ink was coated onto a 50 µm thick PTFE foil (from ANGST+PFISTER, Germany) using a Mayer-rod coating machine (ERICHSEN GmbH & Co. KG, Germany). After drying, electrodes with an active area of 5 cm<sup>2</sup> were punched from the coatings and hot-pressed onto a Nafion® 212 membrane (50 µm, from QUINTECH, Germany) for 3 min at 155 °C at a pressure of 2.5 MPa. The weight of the electrodes was determined by weighing the PTFE foil decals before and after the decal transfer on a microbalance (±15 µg, from METTLER TOLEDO, Germany).

Carbon fiber paper (TGP-H-120 from TORAY, no MPL, 5 wt% PTFE) with a thickness of  $370 \pm 10 \,\mu\text{m}$  was applied as a porous transport layer (PTL) on the cathode side. On the anode, sintered titanium (MOTT CORPORATION, USA) with a porosity of approximately 50 % and a thickness of  $280 \pm 10 \,\mu\text{m}$  was used. The MEA and PTLs were placed between the flow fields of the electrolyzer test cell and sealed with PTFE gaskets (REICHELT, Germany) with an appropriately chosen thickness, such that a compression of  $\approx 25\%$  was achieved for the carbon PTL (assuming the titanium PTL to be incompressible).

### 4.6 Electrochemical Characterization of MEA

An automated test station from GREENLIGHT INNOVATION, equipped with a potentiostat and booster (Reference 3000 and 30 A booster, GAMRY), was used for electrochemical characterization of the MEAs. The cell temperature was fixed to 80 °C and deionized (DI) water was pre-heated to 80 °C and fed to anode and cathode of the electrolysis cell at a rate of 5 ml min<sup>-1</sup>. Both the anode and the cathode side were kept at ambient pressure.

After a warm-up step under  $N_2$  atmosphere, the cell was conditioned at 1 A cm<sup>-2</sup> for 30 min. Subsequently, galvanostatic polarization curves were recorded in a current range from 0.01 to 6 A cm<sup>-2</sup>. At each current, the cell voltage was averaged over 10 s after 5 min equilibration time. Galvanostatic AC impedance measurements between 100 kHz - 1 Hz were carried out

after each polarization step. The amplitude of the current perturbation was chosen for each step to obtain a sufficient signal to noise ratio, while keeping the perturbation small enough to ensure a linear system response. The high-frequency resistance (HFR) was obtained from the high-frequency intercept of the Nyquist plot with the real axis.

## **Supporting Information**

Supporting Information is available from the Wiley Online Library or from the author.

## Acknowledgements

The authors gratefully thank Prof. Dr. Hubert A. Gasteiger for valuable discussions concerning catalyst design, synthesis and electrochemical measurements of catalysts coated membrane electrode assemblies. We furthermore gratefully acknowledge funding by the German Federal Ministry of Education and Research (BMBF) within the Kopernikus Project P2X: Flexible use of renewable resources – research, validation and implementation of 'Power-to-X' concepts. Furthermore, the authors gratefully thank the *e*-conversion Cluster of Excellence (DFG), the Bavarian research networks "Solar Technologies Go Hybrid" and the Center for NanoScience (CeNS) for financial support.

Received: ((will be filled in by the editorial staff))
Revised: ((will be filled in by the editorial staff))
Published online: ((will be filled in by the editorial staff))

## References

- [1] Oberthür, S.; Roche Kelly, C., EU Leadership in International Climate Policy: Achievements and Challenges. *Int. Spect.* **2008**, *43* (3), 35-50.
- [2] Inage, S., The role of large-scale energy storage under high shares of renewable energy. *WIREs Energy Environ.* **2015**, *4* (1), 115-132.
- [3] Barbir, F., PEM electrolysis for production of hydrogen from renewable energy sources. *Sol. Energy* **2005**, *78* (5), 661-669.
- [4] Ayers, K. E.; Capuano, C.; Anderson, E. B., Recent Advances in Cell Cost and Efficiency for PEM-Based Water Electrolysis. *ECS Transactions* **2012**, *41* (10), 15-22.
- [5] Bernt, M.; Hartig-Weiß, A.; Tovini, M. F.; El-Sayed, H. A.; Schramm, C.; Schröter, J.; Gebauer, C.; Gasteiger, H. A., Current Challenges in Catalyst Development for PEM Water Electrolyzers. *Chemie Ingenieur Technik* **2019**, *92*, 31.

- [6] Hagelüken, C., Closing the Loop for Rare Metals Used in Consumer Products:
  Opportunities and Challenges. In *Competition and Conflicts on Resource Use*, Hartard, S.; Liebert, W., Eds. Springer International Publishing: Cham, 2015; pp 103-119.
- [7] Du, Y.; Wang, W.; Zhao, H.; Liu, Y.; Li, S.; Wang, L., The rational doping of P and W in multi-stage catalysts to trigger Pt-like electrocatalytic performance. *J. Mater. Chem. A* **2020**, 8, 25165-25172
- [8] Guo, X.; Xu, Y.; Cheng, Y.; Zhang, Y.; Pang, H., Amorphous cobalt phosphate porous nanosheets derived from twodimensional cobalt phosphonate organic frameworks for high performance of oxygen evolution reaction, *Appl. Mater. Today* **2020**, *18*, 100517
- [9] Yang, M.; Zhou, Y.-N.; Cao, Y.-N.; Tong, Z.; Dong, B.; Chai, Y.-M., Advances and Challenges of Fe-MOFs Based Materials as Electrocatalysts for Water Splitting. *Appl. Mater. Today* **2020**, *20*, 100692
- [10] Xie, J.-Y.; Liu, Z.-Z.; Li, J.; Feng, L.; Yang, M.; Ma, Y.; Liu, D.-P.; Wang, L.; Chai, Y.-M.; Dong, B., Fe-doped CoP core-shell structure with open cages as efficient electrocatalyst for oxygen evolution. *J. Energy Chem.* **2020**, *48*, 328-333
- [11] Duan, Y.; Lee, J. Y.; Xi, S.; Sun, Y.; Ge, J.; Ong, S. J. H.; Chen, Y.; Dou, S.; Meng, F.; Diao, C.; Fisher, A. C.; Wang, X.; Scherer, G. G.; Grimaud, A.; Xu, Z. J., Anodic Oxidation Enabled Cation Leaching for Promoting Surface Reconstruction in Water Oxidation. *Angew. Chem., Int. Ed.* **2021**, *60*, 13, 7418-7425
- [12] Danilovic, N.; Subbaraman, R.; Chang, K.-C.; Chang, S. H.; Kang, Y. J.; Snyder, J.; Paulikas, A. P.; Strmcnik, D.; Kim, Y.-T.; Myers, D.; Stamenkovic, V. R.; Markovic, N. M., Activity–Stability Trends for the Oxygen Evolution Reaction on Monometallic Oxides in Acidic Environments. *J. Phys. Chem. Lett.* **2014**, *5* (14), 2474-2478.
- [13] Cherevko, S.; Geiger, S.; Kasian, O.; Mingers, A.; Mayrhofer, K. J. J., Oxygen evolution activity and stability of iridium in acidic media. Part 2. Electrochemically grown hydrous iridium oxide. *J. Electroanal. Chem.* **2016**, 774, 102-110.
- [14] Liu, P.-Y.; Hsu, C.-C.; Chuang, M.-C., Hemin-mediated construction of iridium oxide with superior stability for the oxygen evolution reaction. *J. Mater. Chem. A* **2017**, *5* (6), 2959-2971.
- [15] Xu, S.; Liu, Y.; Tong, J.; Hu, W.; Xia, Q., Iridium–nickel composite oxide catalysts for oxygen evolution reaction in acidic water electrolysis. *Russ. J. Electrochem.*+ **2016,** *52* (11), 1021-1031.
- [16] Nong, H. N.; Gan, L.; Willinger, E.; Teschner, D.; Strasser, P., IrOx core-shell nanocatalysts for cost- and energy-efficient electrochemical water splitting. *Chem. Sci.* **2014**, *5* (8), 2955-2963.
- [17] González-Huerta, R. G.; Ramos-Sánchez, G.; Balbuena, P. B., Oxygen evolution in Co-doped RuO2 and IrO2: Experimental and theoretical insights to diminish electrolysis overpotential. *J. Power Sources* **2014**, *268*, 69-76.
- [18] Tariq, M.; Zaman, W. Q.; Sun, W.; Zhou, Z.; Wu, Y.; Cao, L.-m.; Yang, J., Unraveling the Beneficial Electrochemistry of IrO2/MoO3 Hybrid as a Highly Stable and Efficient Oxygen Evolution Reaction Catalyst. *ACS Sustain. Chem. Eng.* **2018**, *6* (4), 4854-4862.
- [19] Sardar, K.; Ball, S. C.; Sharman, J. D. B.; Thompsett, D.; Fisher, J. M.; Smith, R. A. P.; Biswas, P. K.; Lees, M. R.; Kashtiban, R. J.; Sloan, J.; Walton, R. I., Bismuth Iridium Oxide Oxygen Evolution Catalyst from Hydrothermal Synthesis. *Chem. Mater.* **2012**, *24* (21), 4192-4200.

- [20] Zlotorowicz, A.; Seland, F.; Sunde, S., Composite Thin Film Iridium- Niobium Oxide Electrocatalysts for the Oxygen Evolution Electrode. *ECS Transactions* **2013**, *50* (36), 71-84.
- [21] Corona-Guinto, J. L.; Cardeño-García, L.; Martínez-Casillas, D. C.; Sandoval-Pineda, J. M.; Tamayo-Meza, P.; Silva-Casarin, R.; González-Huerta, R. G., Performance of a PEM electrolyzer using RuIrCoOx electrocatalysts for the oxygen evolution electrode. *Int. J. Hydrogen Energ.* **2013**, *38* (28), 12667-12673.
- [22] Kadakia, K.; Datta, M. K.; Velikokhatnyi, O. I.; Jampani, P. H.; Kumta, P. N., Fluorine doped (Ir,Sn,Nb)O2 anode electro-catalyst for oxygen evolution via PEM based water electrolysis. *Int. J. Hydrogen Energ.* **2014**, *39* (2), 664-674.
- [23] Kadakia, K. S.; Jampani, P. H.; Velikokhatnyi, O. I.; Datta, M. K.; Patel, P.; Chung, S. J.; Park, S. K.; Poston, J. A.; Manivannan, A.; Kumta, P. N., Study of fluorine doped (Nb,Ir)O2 solid solution electro-catalyst powders for proton exchange membrane based oxygen evolution reaction. *Mater. Sci. Eng. B* **2016**, *212*, 101-108.
- [24] Alia, S. M.; Shulda, S.; Ngo, C.; Pylypenko, S.; Pivovar, B. S., Iridium-Based Nanowires as Highly Active, Oxygen Evolution Reaction Electrocatalysts. *ACS Catal.* **2018**, 8 (3), 2111-2120.
- [25] Li, G.; Yu, H.; Yang, D.; Chi, J.; Wang, X.; Sun, S.; Shao, Z.; Yi, B., Iridium-Tin oxide solid-solution nanocatalysts with enhanced activity and stability for oxygen evolution. *J. Power Sources* **2016**, *325*, 15-24.
- [26] Oh, H.-S.; Nong, H. N.; Reier, T.; Gliech, M.; Strasser, P., Oxide-supported Ir nanodendrites with high activity and durability for the oxygen evolution reaction in acid PEM water electrolyzers. *Chem. Sci.* **2015**, *6* (6), 3321-3328.
- [27] Kim, S.; Cho, M.; Lee, Y., Iridium Oxide Dendrite as a Highly Efficient Dual Electro-Catalyst for Water Splitting and Sensing of H2O2. *J. Electrochem. Soc.* **2017**, *164* (5), B3029-B3035.
- [28] Takimoto, D.; Fukuda, K.; Miyasaka, S.; Ishida, T.; Ayato, Y.; Mochizuki, D.; Shimizu, W.; Sugimoto, W., Synthesis and Oxygen Electrocatalysis of Iridium Oxide Nanosheets. *Electrocatalysis* **2017**, *8* (2), 144-150.
- [29] Zhao, C.; Yifeng, E.; Louzhen, F., Enhanced electrochemical evolution of oxygen by using nanoflowers made from a gold and iridium oxide composite. *Microchim. Acta* **2012**, *178* (1), 107-114.
- [30] Wang, C.; Sui, Y.; Xiao, G.; Yang, X.; Wei, Y.; Zou, G.; Zou, B., Synthesis of Cu-Ir nanocages with enhanced electrocatalytic activity for the oxygen evolution reaction. *J. Mater. Chem. A* **2015**, *3* (39), 19669-19673.
- [31] Slavcheva, E.; Radev, I.; Bliznakov, S.; Topalov, G.; Andreev, P.; Budevski, E., Sputtered iridium oxide films as electrocatalysts for water splitting via PEM electrolysis. *Electrochim. Acta* **2007**, *52* (12), 3889-3894.
- [32] Bernicke, M.; Ortel, E.; Reier, T.; Bergmann, A.; Ferreira de Araujo, J.; Strasser, P.; Kraehnert, R., Iridium Oxide Coatings with Templated Porosity as Highly Active Oxygen Evolution Catalysts: Structure-Activity Relationships. *ChemSusChem* **2015**, 8 (11), 1908-1915.
- [33] Ortel, E.; Reier, T.; Strasser, P.; Kraehnert, R., Mesoporous IrO2 Films Templated by PEO-PB-PEO Block-Copolymers: Self-Assembly, Crystallization Behavior, and Electrocatalytic Performance. *Chem. Mater.* **2011**, *23* (13), 3201-3209.
- [34] Li, G.; Yu, H.; Wang, X.; Yang, D.; Li, Y.; Shao, Z.; Yi, B., Triblock polymer mediated synthesis of Ir–Sn oxide electrocatalysts for oxygen evolution reaction. *J. Power Sources* **2014**, *249*, 175-184.

- [35] Siracusano, S.; Van Dijk, N.; Payne-Johnson, E.; Baglio, V.; Aricò, A. S., Nanosized IrOx and IrRuOx electrocatalysts for the O2 evolution reaction in PEM water electrolysers. *Appl. Catal. B-Environ.* **2015**, *164*, 488-495.
- [36] Böhm, D.; Beetz, M.; Schuster, M.; Peters, K.; Hufnagel, A. G.; Döblinger, M.; Böller, B.; Bein, T.; Fattakhova-Rohlfing, D., Efficient OER Catalyst with Low Ir Volume Density Obtained by Homogeneous Deposition of Iridium Oxide Nanoparticles on Macroporous Antimony-Doped Tin Oxide Support. *Adv. Funct.Mater.* **2020**, *30* (1), 1906670.
- [37] Ayers, K. E.; Renner, J. N.; Danilovic, N.; Wang, J. X.; Zhang, Y.; Maric, R.; Yu, H., Pathways to ultra-low platinum group metal catalyst loading in proton exchange membrane electrolyzers. *Catal. Today* **2016**, *262*, 121-132.
- [38] Nong, H. N.; Oh, H. S.; Reier, T.; Willinger, E.; Willinger, M. G.; Petkov, V.; Teschner, D.; Strasser, P., Oxide-Supported IrNiOx Core—Shell Particles as Efficient, Cost-Effective, and Stable Catalysts for Electrochemical Water Splitting. *Angew. Chem. Int. Edit.* **2015**, *127* (10), 3018-3022.
- [39] Puthiyapura, V. K.; Mamlouk, M.; Pasupathi, S.; Pollet, B. G.; Scott, K., Physical and electrochemical evaluation of ATO supported IrO2 catalyst for proton exchange membrane water electrolyser. *J. Power Sources* **2014**, *269*, 451-460.
- [40] Oh, H.-S.; Nong, H. N.; Strasser, P., Preparation of Mesoporous Sb-, F-, and In-Doped SnO2 Bulk Powder with High Surface Area for Use as Catalyst Supports in Electrolytic Cells. *Adv. Funct. Mater.* **2015**, *25* (7), 1074-1081.
- [41] Puthiyapura, V. K.; Pasupathi, S.; Su, H.; Liu, X.; Pollet, B.; Scott, K., Investigation of supported IrO2 as electrocatalyst for the oxygen evolution reaction in proton exchange membrane water electrolyser. *Int. J. Hydrogen Energ.* **2014**, *39* (5), 1905-1913.
- [42] Yagi, M.; Tomita, E.; Sakita, S.; Kuwabara, T.; Nagai, K., Self-Assembly of Active IrO2 Colloid Catalyst on an ITO Electrode for Efficient Electrochemical Water Oxidation. *J. Phys. Chem. B* **2005**, *109* (46), 21489-21491.
- [43] Karimi, F.; Peppley, B. A., Metal Carbide and Oxide Supports for Iridium-Based Oxygen Evolution Reaction Electrocatalysts for Polymer-Electrolyte-Membrane Water Electrolysis. *Electrochim. Acta* **2017**, *246*, 654-670.
- [44] Polonský, J.; Mazúr, P.; Paidar, M.; Christensen, E.; Bouzek, K., Performance of a PEM water electrolyser using a TaC-supported iridium oxide electrocatalyst. *Int. J. Hydrogen Energ.* **2014**, *39* (7), 3072-3078.
- [45] Geiger, S.; Kasian, O.; Mingers, A. M.; Mayrhofer, K. J. J.; Cherevko, S., Stability limits of tin-based electrocatalyst supports. *Sci. Rep.* **2017**, *7* (1), 4595.
- [46] Trasatti, S., Electrocatalysis: understanding the success of DSA®. *Electrochim. Acta* **2000**, *45* (15), 2377-2385.
- [47] Reier, T.; Weidinger, I.; Hildebrandt, P.; Kraehnert, R.; Strasser, P., Electrocatalytic Oxygen Evolution Reaction on Iridium Oxide Model Film Catalysts: Influence of Oxide Type and Catalyst Substrate Interactions. *ECS Transactions* **2013**, *58* (2), 39-51.
- [48] Reier, T.; Teschner, D.; Lunkenbein, T.; Bergmann, A.; Selve, S.; Kraehnert, R.; Schlögl, R.; Strasser, P., Electrocatalytic Oxygen Evolution on Iridium Oxide: Uncovering Catalyst-Substrate Interactions and Active Iridium Oxide Species. *J. Electrochem. Soc.* **2014**, *161* (9), F876-F882.
- [49] Mazúr, P.; Polonský, J.; Paidar, M.; Bouzek, K., Non-conductive TiO2 as the anode catalyst support for PEM water electrolysis. *Int. J. Hydrogen Energ.* **2012**, *37* (17), 12081-12088.

- [50] Oakton, E.; Lebedev, D.; Povia, M.; Abbott, D. F.; Fabbri, E.; Fedorov, A.; Nachtegaal, M.; Copéret, C.; Schmidt, T. J., IrO2-TiO2: A High-Surface-Area, Active, and Stable Electrocatalyst for the Oxygen Evolution Reaction. *ACS Catal.* **2017**, *7* (4), 2346-2352.
- [51] Yoo, H.; Oh, K.; Lee, Y. R.; Row, K. H.; Lee, G.; Choi, J., Simultaneous co-doping of RuO2 and IrO2 into anodic TiO2 nanotubes: A binary catalyst for electrochemical water splitting. *Int. J. Hydrogen Energ.* **2017**, *42* (10), 6657-6664.
- [52] Hao, C.; Lv, H.; Zhao, Q.; Li, B.; Zhang, C.; Mi, C.; Song, Y.; Ma, J., Investigation of V-doped TiO2 as an anodic catalyst support for SPE water electrolysis. *Int. J. Hydrogen Energ.* **2017**, *42* (15), 9384-9395.
- [53] Hufnagel, A. G.; Häringer, S.; Beetz, M.; Böller, B.; Fattakhova-Rohlfing, D.; Bein, T., Carbon-templated conductive oxide supports for oxygen evolution catalysis. *Nanoscale* **2019**, *11* (30), 14285-14293.
- [54] Hu, W.; Chen, S.; Xia, Q., IrO2/Nb–TiO2 electrocatalyst for oxygen evolution reaction in acidic medium. *Int. J. Hydrogen Energ.* **2014**, *39* (13), 6967-6976.
- [55] PI, H. X.; Newton, M., High-Performance, Long-Lifetime Catalysts for Proton Exchange Membrane Electrolysis. *NREL project report PD103* **2015**.
- [56] Bele, M.; Stojanovski, K.; Jovanovič, P.; Moriau, L.; Koderman Podboršek, G.; Moškon, J.; Umek, P.; Sluban, M.; Dražič, G.; Hodnik, N.; Gaberšček, M., Towards Stable and Conductive Titanium Oxynitride High-Surface-Area Support for Iridium Nanoparticles as Oxygen Evolution Reaction Electrocatalyst. *ChemCatChem* **2019**, *11* (20), 5038-5044.
- [57] Lu, Z.-X.; Shi, Y.; Yan, C.-F.; Guo, C.-Q.; Wang, Z.-D., Investigation on IrO2 supported on hydrogenated TiO2 nanotube array as OER electro-catalyst for water electrolysis. *Int. J. Hydrogen Energ.* **2017**, *42* (6), 3572-3578.
- [58] Siracusano, S.; Baglio, V.; D'Urso, C.; Antonucci, V.; Aricò, A. S., Preparation and characterization of titanium suboxides as conductive supports of IrO2 electrocatalysts for application in SPE electrolysers. *Electrochim. Acta* **2009**, *54* (26), 6292-6299.
- [59] Bernsmeier, D.; Bernicke, M.; Schmack, R.; Sachse, R.; Paul, B.; Bergmann, A.; Strasser, P.; Ortel, E.; Kraehnert, R., Oxygen Evolution Catalysts Based on Ir–Ti Mixed Oxides with Templated Mesopore Structure: Impact of Ir on Activity and Conductivity. *ChemSusChem* **2018**, *11* (14), 2367-2374.
- [60] Bernicke, M.; Bernsmeier, D.; Paul, B.; Schmack, R.; Bergmann, A.; Strasser, P.; Ortel, E.; Kraehnert, R., Tailored mesoporous Ir/TiOx: Identification of structure-activity relationships for an efficient oxygen evolution reaction. *J. Catal.* **2019**, *376*, 209-218.
- [61] Oakton, E.; Lebedev, D.; Fedorov, A.; Krumeich, F.; Tillier, J.; Sereda, O.; Schmidt, T. J.; Copéret, C., A simple one-pot Adams method route to conductive high surface area IrO2–TiO2 materials. *New J. Chem.* **2016**, *40* (2), 1834-1838.
- [62] Bernt, M.; Gasteiger, H. A., Influence of Ionomer Content in IrO2/TiO2 Electrodes on PEM Water Electrolyzer Performance. *J. Electrochem. Soc.* **2016**, *163* (11), F3179-F3189.
- [63] Lopez, M.; Schleunung, A.; Biberbach, P., Precious metal oxide catalyst for water electrolysis. (Umicore AG) U.S. 7,976,989B2, **2004**
- [64] Geiger, S.; Kasian, O.; Shrestha, B. R.; Mingers, A. M.; Mayrhofer, K. J. J.; Cherevko, S., Activity and Stability of Electrochemically and Thermally Treated Iridium for the Oxygen Evolution Reaction. *J. Electrochem. Soc.* **2016**, *163* (11), F3132-F3138.
- [65] Vuković, M., Voltammetric and galvanostatic studies of hydrous and anhydrous iridium oxide films. *J. Appl. Electrochem.* **1990,** *20* (6), 969-973.

- [66] Vuković, M., Oxygen evolution reaction on thermally treated iridium oxide films. *J. Appl. Electrochem.* **1987**, *17* (4), 737-745.
- [67] Abbott, D. F.; Lebedev, D.; Waltar, K.; Povia, M.; Nachtegaal, M.; Fabbri, E.; Copéret, C.; Schmidt, T. J., Iridium Oxide for the Oxygen Evolution Reaction: Correlation between Particle Size, Morphology, and the Surface Hydroxo Layer from Operando XAS. *Chem. Mater.* **2016**, *28* (18), 6591-6604.
- [68] Cruz, J. C.; Baglio, V.; Siracusano, S.; Ornelas, R.; Ortiz-Frade, L.; Arriaga, L. G.; Antonucci, V.; Aricò, A. S., Nanosized IrO2 electrocatalysts for oxygen evolution reaction in an SPE electrolyzer. *J. Nanopart. Res.* **2011**, *13* (4), 1639-1646.
- [69] Balachandran, U.; Eror, N. G., Raman spectra of titanium dioxide. *J. Solid State Chem.* **1982**, 42 (3), 276-282.
- [70] Korotcov, A. V.; Huang, Y. S.; Tiong, K. K.; Tsai, D. S., Raman scattering characterization of well-aligned RuO2 and IrO2 nanocrystals. *J. Raman Spectrosc.* **2007**, *38* (6), 737-749.
- [71] Huang, Y. S.; Lin, S. S.; Huang, C. R.; Lee, M. C.; Dann, T. E.; Chien, F. Z., Raman spectrum of IrO2. *Solid State Commun.* **1989**, *70* (5), 517-522.
- [72] Povia, M.; Abbott, D. F.; Herranz, J.; Heinritz, A.; Lebedev, D.; Kim, B.-J.; Fabbri, E.; Patru, A.; Kohlbrecher, J.; Schäublin, R.; Nachtegaal, M.; Copéret, C.; Schmidt, T. J., Operando X-ray characterization of high surface area iridium oxides to decouple their activity losses for the oxygen evolution reaction. *Energy Environ. Sci.* **2019**, *12* (10), 3038-3052.
- [73] Felix, C.; Bladergroen, B. J.; Linkov, V.; Pollet, B. G.; Pasupathi, S., Ex-Situ Electrochemical Characterization of IrO2 Synthesized by a Modified Adams Fusion Method for the Oxygen Evolution Reaction. *Catalysts* **2019**, *9* (4), 318.
- [74] Patterson, A. L., The Scherrer Formula for X-Ray Particle Size Determination. *Phys. Rev.* **1939**, *56* (10), 978-982.
- [75] Gimenez, P.; Fereres, S., Effect of Heating Rates and Composition on the Thermal Decomposition of Nitrate Based Molten Salts. *Enrgy. Proced.* **2015**, *69*, 654-662.
- [76] Yoshio, H.; Taizo, U.; Osami, A., The Thermal Decomposition of Sodium Nitrate and the Effects of Several Oxides on the Decomposition. *B. Chem. Soc. Jpn.* **1981,** *54* (5), 1385-1391.
- [77] Guire, M. R.; Hu, M. Z.; Gogotsi, Y.; Lu, S. W., Ceramic Nanomaterials and Nanotechnology II: Proceedings of the symposium held at the 105th Annual Meeting of The American Ceramic Society, April 27-30, in Nashville, Tennessee, Ceram. Trans., Wiley, 2004.
- [78] Burke, L.D., Whelan, D.P., A new interpretation of the charge storage and electrical conductivity behaviour of hydrous iridium oxide. *J. Electroanal. Chem.* **1981**, *124*, 333-337.
- [79] Sugimoto, W.; Iwata, H.; Yokoshima, K.; Murakami, Y.; Takasu, Y.; Proton and Electron Conductivity in Hydrous Ruthenium Oxides Evaluated by Electrochemical Impedance Spectroscopy: The Origin of Large Capacitance. *J. Phys. Chem. B*, **2005**, *109* (15), 7330–7338.
- [80] Aurian-Blajeni, B.; Beebe, X.; Rauh, R.D.; Rose, T.L., Impedance of hydrated iridium oxide electrodes. *Electrochimica Acta* **1989**, *34*, 6, 795-802
- [81] Ping, Y.; Gall, G.; Goddard III, W. A., Electronic Structure of IrO2: The Role of the Metal d Orbitals. *J. Phys. Chem. C* **2015**, *119*, 21, 11570–11577
- [82] Chow, K.-F.; Carducci, T. M.; Murray, R. W., Electronic Conductivity of Films of Electroflocculated 2 nm Iridium Oxide Nanoparticles. *J. Am. Chem. Soc.* **2014**, *136* (9), 3385-3387.

- [83] Ohno, H.; Nohara, S.; Kakinuma, K.; Uchida, M.; Uchida, H., Effect of Electronic Conductivities of Iridium Oxide/Doped SnO2 Oxygen-Evolving Catalysts on the Polarization Properties in Proton Exchange Membrane Water Electrolysis. *Catalysts* **2019**, *9* (1), 74.
- [84] Lim, J.; Park, D.; Jeon, S. S.; Roh, C. W.; Choi, J.; Yoon, D.; Park, M.; Jung, H.; Lee, H., Ultrathin IrO2 Nanoneedles for Electrochemical Water Oxidation. *Adv. Funct. Mater.* **2018**, 28 (4), 1704796.
- [85] Ouattara, L.; Fierro, S.; Frey, O.; Koudelka, M.; Comninellis, C., Electrochemical comparison of IrO2 prepared by anodic oxidation of pure iridium and IrO2 prepared by thermal decomposition of H2IrCl6 precursor solution. *J. Appl. Electrochem.* **2009**, *39* (8), 1361-1367.
- [86] Juodkazytė, J.; Šebeka, B.; Valsiunas, I.; Juodkazis, K., Iridium Anodic Oxidation to Ir(III) and Ir(IV) Hydrous Oxides. *Electroanal.* **2005**, *17* (11), 947-952.
- [87] Godínez-Salomón, F.; Albiter, L.; Alia, S. M.; Pivovar, B. S.; Camacho-Forero, L. E.; Balbuena, P. B.; Mendoza-Cruz, R.; Arellano-Jimenez, M. J.; Rhodes, C. P., Self-Supported Hydrous Iridium—Nickel Oxide Two-Dimensional Nanoframes for High Activity Oxygen Evolution Electrocatalysts. *ACS Catal.* **2018**, *8* (11), 10498-10520.
- [88] Xu, W.; Haarberg, G. M.; Sunde, S.; Seland, F.; Ratvik, A. P.; Zimmerman, E.; Shimamune, T.; Gustavsson, J.; Åkre, T., Calcination Temperature Dependent Catalytic Activity and Stability of IrO2 –Ta2O5 Anodes for Oxygen Evolution Reaction in Aqueous Sulfate Electrolytes. *J. Electrochem. Soc.* **2017**, *164* (9), F895-F900.
- [89] Minguzzi, A.; Lugaresi, O.; Achilli, E.; Locatelli, C.; Vertova, A.; Ghigna, P.; Rondinini, S., Observing the oxidation state turnover in heterogeneous iridium-based water oxidation catalysts. *Chem. Sci.* **2014**, *5* (9), 3591-3597.
- [90] Bernt, M.; Siebel, A.; Gasteiger, H. A., Analysis of Voltage Losses in PEM Water Electrolyzers with Low Platinum Group Metal Loadings. *J. Electrochem. Soc.* **2018**, 165, F305.
- [91] M. Bernt, C. Schramm, J. Schröter, C. Gebauer, J. Byrkness, C. Eickes, H.A. Gasteiger; Effect of the IrOx Conductivity on the Anode Electrode / Porous Transport Layer Interfacial Resistance in PEM Water Electrolyzers. manuscript to be submitted.
- [92] Adams, R.; Shriner, R. L., Platinum Oxide as a Catalyst in the Reduction of Organic Compounds. III. Preparation and Properties of the Oxide of Platinum Obtained by the Fusion of Chloroplatinic Acid with Sodium Nitrate. *J. Am. Chem. Soc.* **1923**, *45* (9), 2171-2179.